Modeling of Fuel Cell Cold Start and Dimension Reduction Simplification Method

Journal of The Electrochemical Society, 2020 **167** 044501
1945-7111/2020/167(4)/044501/17/$40.00 © 2020 The Electrochemical Society ("ECS"). Published on behalf of ECS by IOP Publishing Limited

Modeling of Fuel Cell Cold Start and Dimension Reduction Simplification Method

Hongliang Jiang,[1,2] Liangfei Xu,[1,z] Henning Struchtrup,[2] Jianqiu Li,[1] Quanquan Gan,[3] Xin Xu,[3] Zunyan Hu,[1] and Minggao Ouyang[1]

[1]*State Key Laboratory of Automotive Safety and Energy, Department of Automotive Engineering, Tsinghua University, Beijing 100084, People's Republic of China*
[2]*Institute for Integrated Energy Systems and Department of Mechanical Engineering, University of Victoria, Victoria, British Columbia V8W 3P6, Canada*
[3]*Shanghai Shen-li High Tech Co., Ltd, Industry Comprehensive Development Zone, Shanghai, People's Republic of China*

Sub-zero startup ability remains a key barrier for commercial application of polymer electrolyte fuel cells (PEMFC), especially for automotive applications. In order to improve the startup ability and durability of fuel cells, understanding of the characteristics and mechanisms of cold start is essential, and here modeling of fuel cell cold start plays an important role. In this study, a one-dimensional model is developed to simulate the fuel cell cold start. The model includes mass transport and phase change, heat transfer and electrochemical reaction. Key features such as membrane water and local current distributions are analyzed. Based on the one-dimensional model and simulation results, a spatial reduced simplified model is developed that distinguished only n states across the cell. The simplified model inherits the key features of the one-dimensional model, while the computational cost is significantly reduced to 10% (from 216 s to 20.88 s). The one-dimensional model and simplified model are both validated by the cold start experiment and the voltage error and temperature error are within 15% and 1.2 K respectively. Thus, the proposed simplified model could be used in dynamic simulation and in further multi-scale modeling study to build a stack model.
 [DOI: 10.1149/1945-7111/ab6ee7]

Manuscript submitted October 28, 2019; revised manuscript received January 13, 2020. Published February 11, 2020.

Abbreviations

ACL	anode catalyst layer
BP	bipolar plate
CCL	cathode catalyst layer
CL	catalyst layer
GDL	gas diffusion layer
HOR	hydrogen oxidation reaction
MPL	multi porous media
PEM	polymer electrolyte membrane
PEMFC	polymer electrolyte membrane fuel cell
ORR	oxygen reduction reaction

Roman

a	activity of water
A	area of the cell, m^2
c	molar concentration of species, mol/m^3
c_p	thermal capacity, $J/kg \cdot K$
D	diffusivity, $m^2 \cdot s^{-1}$
$\vec{d}$	diffusive gradient
E	potential
EW	equivalent weight of membrane, kg/mol
F	Faraday constant, 96485 C/mol
h	transport coefficient at gas channel and porous media interface, m/s
$\triangle h$	latent heat, J/kg
I	current density, A/m^2
J	molar flux per unit area, mol/m^2s
$\vec{j}$	mass flux vector, $kg/m^2 \cdot s$
j	local current density, A/m^3
j_0	exchange current density, A/m^3
k	thermal conductivity, $W/m \cdot K$
L	length, m
M	molar mass, kg/mol
N	gas flux of gas channel, mol/s
p	pressure, Pa
R	universal gas constant, 8.314 J $mol^{-1} \cdot K^{-1}$ ohmic resistance, $\Omega \cdot m^2$
S	source term
$\triangle S$	entropy change, $J/mol \cdot K$
s	volume fraction
T	temperature, K
t	time, s
$\vec{u}$	velocity vector, m/s
V	voltage, V
W	width, m
x	molar fraction

Greek

α	transfer coefficient/gas supply stoichiometric ratio
β	proportion of first part of catalyst area closer to membrane
γ	phase change coefficient
δ	thickness, m
ε	porosity
η	overpotential, V
θ	correction factor for membrane water distribution
κ	permeability, m^2
λ	membrane water content
μ	dynamic viscosity, $Pa \cdot s$
ρ	density, kg/m^3
σ	conductivity, S/m
ϕ	potential, V
ω	mass fraction

Subscripts and superscripts

a	anode
agc	anode gas channel
atm	atmosphere
bp	bipolar plate
c	cathode
cc	coolant channel
cell	average value of the cell

[z]E-mail: xuliangfei@tsinghua.edu.cn

cgc	cathode gas channel
c, rib	coolant channel rib
d	diffusion
e	electro osmotic drag
eff	effective
ele	electrical
eq	equilibrium
evap	evaporation heat
F	freezing point
fusion	fusion heat
gc	gas channel
H_2	hydrogen
H_2O	water
in	inlet flux
ion	ionic/ionomer
m	mass
mem	membrane
mw	membrane water
m − v	from membrane water to vapor
m − i	from membrane water to ice
N_2	nitrogen
O_2	oxygen
out	outlet flux
ref	reference state
rib	gas channel rib
sat	saturation
v	vapor
v − i	from vapor to ice
w	water

Polymer electrolyte membrane fuel cells (PEMFC) are considered as the most promising fuel cells for automotive application, due to their high power density, low operation temperature and zero emission. Cost, durability and cold start ability still remain obstacles to fuel cell vehicle commercialization.[1–4] Engines for automobiles are required to have the ability of starting up and operating in sub-zero temperature environment, which makes cold start one of the main barriers to commercial application of PEMFC. According to Department of Energy (DOE) reports, the target for fuel cell cold start by 2020 is unassisted cold start from −30 °C, assisted startup from −40 °C, and startup to 50% rated power within 30 s from −20 °C.[5] In the past decade, technical progress has been made in fuel cell cold start. For example, the fuel cell products used in Toyota FCHV-adv, Mirai and Honda Clarity both have the cold start ability from −30 °C.[6–8] However, the influence of cold start on durability remains unclear, in which ice formation and distribution in PEMFC plays an important role.

Water plays an important role in operation of PEMFC. Water is produced by electrochemical reaction of hydrogen and oxygen, at the same time as electricity and heat are generated. Water is also necessary since the polymer electrolyte membrane needs to be well hydrated in order to have high proton conductivity. However, in subzero temperature, water produced in the fuel cell may freeze inside the porous medium, which may hinder the transport of reactant and reduce the electrochemical active area. The key issues during cold start are temperature rise and ice formation. A successful cold start requires to heat up the fuel cell before mass transport and electrochemical reaction are totally blocked by ice.

Early research on fuel cell cold start was mainly experimental research focusing on the impact factors on the cold start ability and the mechanism. Hishinuma et al. performed cold start experiments with fuel cells in 2004 at temperatures from −3 °C to −25 °C and pressures from 1 to 2 atmospheres.[9] At the time, self-starting succeeded only from above −5 °C. Main factors that influence cold start performance were identified in experiments by Oszcipok et al., Yan et al. and Tajiri et al.[10–14] Temperature and initial water content have significant influence on cold start performance, where higher startup temperature and lower initial water content facilitate successful cold start. With lower initial membrane water content, water produced by the reaction is absorbed into the membrane at the beginning of cold start, which will reduce the ice formation. The influence of reactant gas flow rate is complex. Higher gas flow rate can help avoiding voltage dropping to zero, and remove more water vapor from the fuel cell. On the other hand, lower voltage resulted from reactant starvation, which implies higher production of heat. Pumping hydrogen caused by oxygen starvation also produced more heat. Reactant starvation and pumping hydrogen heat are useful in developing rapid startup strategy.[7]

Microprocesses inside the fuel cells during cold start and their influence on reaction are another focus of research. Ice was observed in membrane electrode assembly (MEA) and the gas diffusion layer (GDL) in Yan's experiment through scanning electron microscopy (SEM),[12] and in Ge et al.'s experiment through in situ imaging.[15,16] Under different operating conditions, ice appears in different regions of the catalyst layer during cold start in Tabe et al.'s experiment,[17] indicating that ice distribution in the proton transport direction is important. Other parameters were also studied to help understand the mechanism, such as electrochemical active surface area (ECSA) and high frequency resistance (HFR). Ge et al.'s experiment[18] showed that ECSA decreased during cold start, indicating ice might form between Pt particles and ionomer in cathode catalyst layer (CL). On the contrary, no ECSA decrease was observed at the anode side. HFR is usually used to represent the water content of the membrane. In Tajiri et al.'s experiment, HFR decreased at first and reached a stable value before shutdown.[14] This indicated that the membrane was hydrated at first and then reached a saturation value before shutdown. Based on the state of water in the cell, Wang defined three stages of fuel cell cold start: membrane hydration, ice formation and residual ice melting.[19] Super-cooled water may also exist during the cold start.[17,20–22] However, super-cooled water is more likely to exist at temperature close to zero, e.g., at or above −10 °C, and its behavior is stochastic.[17] It is still difficult to use in improving cold start ability.

Modeling is an important method to understand the mechanisms in fuel cell cold start and also provides a tool to study cold start strategies. Analytical models are efficient tools in describing the mechanism of fuel cell cols start, including heat generation, water production and phase change etc Mao et al. proposed an analytical model, based on which they elucidated the cold start behaviors of a PEFC from −10 °C and −20 °C and identified key parameters controlling PEFC cold start.[23] Wang also analyzed the key parameters in the fuel cell cold start using an analytical model.[24] Time constant was used in the model to describe the transient of water phase change. Base on the analysis results of water behaviors of the analytical model, He also characterized fuel cell cold start as a three stages process.[19] Analytical models are also useful in estimating the temperature rise and ice formation, and also the cold start ability of a fuel cell. In Ge et al.'s research[16] and Huang's research,[25] analytical models of water production and heat generation were used to estimate the water uptake capability, and then estimate the cold start ability of certain fuel cells.

Microscopic models of fuel cell cold start focused on water phase change in porous media in sub-zero condition. Dursch et al. developed microscopic models to study the ice crystallization and melting kinetics.[26–28] Ishikawa et al. used microscopic model to analyze supercooled states of water generated below the freezing point in a PEFC theoretically and compare with experiment results.[29]

Numerical models, especially three dimensional models, are powerful tools to analyze the characteristic of fuel cell cold start, especially three dimensional spatial distribution characteristics. These models are usually used in explaining experimental results and then improving cell design. Mao, Jiang and Wang et al. developed a three dimensional multiphase model for cold start of fuel cell[30,31] in 2007. Water existed as vapor or ice in the model, and the influence of ice on mass transport and electrochemical reaction was considered. Ice fraction was introduced to describe the amount of ice, similar to water flooding in normal temperature operation, where equilibrium ice formation and melting is assumed. A 100 cm single channel cell unit was simulated and results validated with experimental data. Jiao and Li et al. introduced liquid water and

frozen membrane water so that there were five states of water in their model.[32] Non-equilibrium phase change was used in the model, and the phase change rate between different kinds of water was modelled as a linear relationship. Both their simulations showed strong nonuniformity of temperature, water content and ice fraction in the through-plane direction.

Three dimensional computational fluid dynamics (CFD) models can describe the details of the cold start and the complete distribution of the internal states. However, they also require high computational effort, even though the computational domain is just a small slice of the cell. Each simulation case of a stack model developed by Macedo-Valencia et al. with 6 cells and 31.2 cm^2area took around 24 h on a workstation.[33] For further applications, simulations of large area cells and stack models are required, which are almost impossible to build using 3D CFD method.

Lower dimensional models have a clear advantage in computational cost, while some details are neglected. In two dimensional cold start models, usually through-plate direction and along channel direction are studied,[34] or the through-plane direction and channel-rib direction are studied.[35–37] In one-dimensional models, only the through-plane direction is studied since it is most important.[23,38,39] Some of the one-dimensional models only considered heat transfer and were extended to stack modesl.[40–42] In order to develop a stack model, Zhou et al. only studied the through-plane direction and did not solve the charge conservation equation.[43]

Thus, in order to balance the model detail and computational efficiency, a one-dimensional model is suitable for modeling study of single cell cold start, and for further extension to stack models, simpler model is also needed. Zeros dimensional models are suitable for state observation and control.[44–46] Usually a one-dimensional CFD model of a single cell is simplified into a zero-dimensional model, in which lumped values of internal states of the functional layers in through plate direction are studied. Fang proposed a long channel cell model and a stack model by integrating a zero-dimensional model.[47] In order to study the water transport phenomena in membrane and GDL, a steady-state analytical solution of two-phase water distribution in membrane and GDL by Hu et al.[48] was used in the zero-dimensional model of Fang, while the CLs were considered as points in the model. Tang et al. also developed a stack model through spatial resolution method to study fuel cell stack cold start based on a lumped model of the functional layers.[49] However, in existing zero-dimensional models of single cell, distributions of internal states in CL were not modeled. From the existing literatures, simulations and experiments results showed strong nonuniformity of reaction rate, water content and ice saturation distribution in CL during cold start process.[17,30,32,50] Neglecting these distributions will cause error of the cold start model. Thus, the purpose of this study is to describe the distribution of internal states in a simplified zero-dimensional model. The target is to developed a simplified single cell model with small error comparing to one-dimensional model and without increasing computational cost significantly.

In order to establish a simplified model that inherits distribution features of one-dimensional model, a one-dimensional model for fuel cell cold start is developed as a baseline model. Through analyzing the results of the one-dimensional model, characteristics of fuel cell cold start are concluded as the guidance of model simplification. Then model simplification is conducted and a simplified cold start model is developed. In particular, CL is considered as two parts in the model according to the simulation results of the baseline model. The developed simplified model is simulated under different operation conditions. Simulation results are analyzed and compared with baseline model and experimental data to validate its validity and effectiveness.

One-Dimensional Cold Start Model

In this section, a one-dimensional (1D) transient model of PEMFC cold start is developed referring to previous modeling study.[32,50] Figure 1 shows the major physics and chemical process considered in this model, including electrochemical reaction, charge transport, mass transport and phase change, heat transfer etc. Only the direction normal to the membrane surface (through-plane direction) is studied. Note that the size scale in the figure is not the actual scale. Parameters are given in Table I.

Electrochemical reaction and charge transport.—In fuel cells, hydrogen oxidation reaction (HOR) and oxygen reduction reaction (ORR) take place in anode CL and cathode CL respectively. Reaction kinetics of both reactions is generally described by the Butler–Volmer equation (B-V equation), where local reaction rates at anode CL and cathode CL are

$$j = (1 - s_{\text{ice}})j_{0,\text{a}}\frac{c_{\text{H}_2}}{c_{\text{H}_2,\text{ref}}}\left[\exp\left(\frac{\alpha_\text{a}F\eta}{RT}\right) - \exp\left(-\frac{\alpha_\text{c}F\eta}{RT}\right)\right] \quad [1]$$

$$j = (1 - s_{\text{ice}})j_{0,\text{c}}\frac{c_{\text{O}_2}}{c_{\text{O}_2,\text{ref}}}\left[\exp\left(\frac{\alpha_\text{a}F\eta}{RT}\right) - \exp\left(-\frac{\alpha_\text{c}F\eta}{RT}\right)\right] \quad [2]$$

where in normal operation $j > 0$ at the anode and $j < 0$ at the cathode. Here, s_{ice} is the ice volume fraction in the catalyst layer and the influence of ice on the active surface is assumed as linear. Moreover, a_a and a_c are the original active surface area of anode and cathode, respectively, while $j_{0,\text{a}}$ and $j_{0,\text{c}}$ are exchange current density in anode and cathode, respectively. The exchange current densities are functions of temperature, and $j_{0,\text{c}} \ll j_{0,\text{a}}$ due to the slow ORR. c_{H_2} is the local hydrogen concentration and $c_{\text{H}_2,\text{ref}}$ is the reference concentration. Furthermore, c_{O_2} is the local oxygen concentration and $c_{\text{O}_2,\text{ref}}$ is the reference concentration, α_a and α_c are charge transport coefficients that must be determined experimentally, and $T$is the local temperature. The overpotential

η is defined as

$$\eta = \phi_{ele} - \phi_{ion} - E_{eq} \quad [3]$$

where ϕ_{ele} is electric potential, ϕ_{ion} is ionic potential, and E_{eq} is the equilibrium potential, with a reference value of zero at the anode. Equilibrium potential in cathode is determined by Nernst Equation.

$$E_{\text{eq},c} = 1.229\text{V} - 0.9 \times 10^{-3}\text{V/K} \times (T - 298\ \text{K}) + \frac{RT}{2F}\ln(p_{\text{H}_2} \cdot p_{\text{O}_2}^{0.5}) \quad [4]$$

Charge transport in fuel cell includes proton transport and electron transport, where charge conservation is expressed as

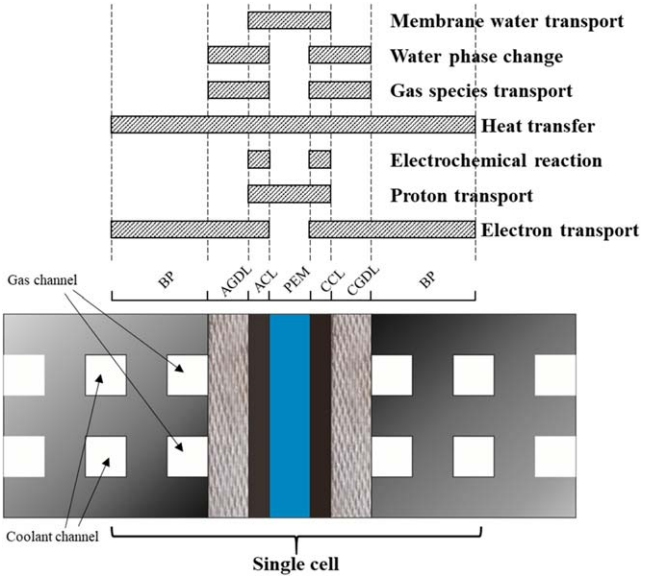

Figure 1. Schematic of a single fuel cell and the major physics and chemical process considered in the model.

Table I. Model parameters.

Parameter	Value
Universal gas constant	$R = 8.314\ \mathrm{J \cdot mol^{-1}K^{-1}}$
Faraday constant	$F = 96485\ \mathrm{C \cdot mol^{-1}}$
Atmosphere pressure	$p_{\mathrm{atm}} = 101.3\ \mathrm{kPa}$
Molar mass of oxygen, hydrogen, water, nitrogen	$M_{\mathrm{O_2,H_2,H_2O,N_2}} = 0.032, 0.002, 0.018, 0.028\ \mathrm{kg \cdot mol^{-1}}$
Densities of dry membrane, GDL, CL, BP	$\rho_{\mathrm{mem,\ gdl,\ cl,\ bp}} = 1980, 1000, 1000, 1000\ \mathrm{kg \cdot m^3}$
Densities of coolant, ice	$\rho_{\mathrm{coolant,ice}} = 990, 920\ \mathrm{kg \cdot m^3}$
Equivalent weight of membrane	$EW = 1.1\ \mathrm{kg \cdot mol^{-1}}$
Gas channel length, width, rib width, depth	$L_{\mathrm{gc}}, W_{\mathrm{gc}}, W_{\mathrm{rib}}, H_{\mathrm{gc}} = 300, 1, 1, 0.4\ \mathrm{mm}$
Coolant channel width, rib width, depth, bipolar plate thickness	$W_{\mathrm{cc}}, W_{\mathrm{c,rib}}, \delta_{\mathrm{cc}}, \delta_{\mathrm{bp}} = 1, 1, 0.4, 2\ \mathrm{mm}$
Thickness of membrane, CL, GDL	$\delta_{\mathrm{mem}}, \delta_{\mathrm{cl}}, \delta_{\mathrm{gdl}} = 15, 15, 230\ \mu\mathrm{m}$
Porosities of CL, GDL, ionomer fraction in CL	$\varepsilon_{\mathrm{cl,\ gdl,\ ion}} = 0.5,\ 0.6,\ 0.2$
Specific heat capacities of membrane, coolant, GDL, CL, BP	$(c_p)_{\mathrm{m,\ coolant,\ gdl,\ cl,\ bp}} = 833, 3200, 568, 3300, 1580\ \mathrm{J \cdot kg^{-1} \cdot K^{-1}}$
Thermal conductivities of membrane, coolant, GDL, CL, BP	$k_{\mathrm{mem,coolant,gdl,cl,bp}} = 0.95, 0.6, 1, 1, 20\ \mathrm{W \cdot m^{-1} \cdot K^{-1}}$
Latent heat of water evaporation and fusion	$h_{\mathrm{evap,fusion}} = 2438.5T + 3.1707 \times 10^6, 3.336 \times 10^5\ \mathrm{J \cdot kg^{-1}}$
Transport coefficients at the GDL/GC interface of vapor, oxygen	$h_{\mathrm{gc,v}} = 0.8\ \mathrm{m \cdot s^{-1}}, h_{\mathrm{gc,O_2}} = 0.08\ \mathrm{m \cdot s^{-1}}$
Diffusivities of gas species	$D_{(\mathrm{H_2,H_2O}),\ (\mathrm{N_2,H_2O}),\ (\mathrm{O_2,H_2O}),\ (\mathrm{O_2,N_2})} = (9.15,\ 2.56,\ 2.82,\ 2.2) \times 10^{-5} \times (T/307.1\mathrm{K})^{1.75}\mathrm{m^2 \cdot s^{-1}}$
Dynamic viscosities of gas mixture in anode cathode	$\mu_{a,\mathrm{c}} = 9.88 \times 10^{-6}, 15.3 \times 10^{-6}\ \mathrm{Pa \cdot s}$
Permeabilities of gas mixture in CL, GDL	$\kappa_{\mathrm{cl,\ gdl}} = 1 \times 10^{-13}, 1 \times 10^{-12}\ \mathrm{m^2}$
Phase change rate coefficients	$\gamma_{\mathrm{m-v,\ m-i,\ v-i}} = 0.1, 1, 1\ \mathrm{s^{-1}}$
Gas channel outlet coefficients	$k_{(\mathrm{agc,out}),\ (\mathrm{cgc,out})} = (0.2,\ 5) \times 10^{-11}\mathrm{kg \cdot s^{-1} \cdot Pa^{-1}}$
Reference concentration of oxygen and hydrogen in B-V equation	$c_{\mathrm{O_2,ref}} = 40\ \mathrm{mol \cdot m^3}, c_{\mathrm{H_2,ref}} = 40\ \mathrm{mol \cdot m^3}$
Transport coefficients in anode reaction	$\alpha_{\mathrm{a}} = \alpha_{\mathrm{c}} = 1$
Transport coefficients in cathode reaction	$\alpha_{\mathrm{a}} = 3, \alpha_{\mathrm{c}} = 1$
Volumetric exchange current in anode and cathode	$j_{0,\mathrm{a}} = 1 \times 10^9 \times e^{[-1400 \times (1/T - 1/353.15\mathrm{K})]}\ j_{0,\mathrm{c}} = 1 \times 10^4 \times e^{[-7900 \times (1/T - 1/353.15\mathrm{K})]}$
Electric conductivities of GDL, CL, BP	$(\sigma_{\mathrm{ele}})_{\mathrm{gdl,cl,bp}} = 300, 300, 20000\ \mathrm{S \cdot m^{-1}}$

$$-\nabla \cdot (\sigma_{\mathrm{ion}}^{\mathrm{eff}} \nabla \phi_{\mathrm{ion}}) = S_{\mathrm{ion}} \quad [5]$$

$$-\nabla \cdot (\sigma_{\mathrm{ele}}^{\mathrm{eff}} \nabla \phi_{\mathrm{ele}}) = S_{\mathrm{ele}} \quad [6]$$

Effective electron conductivity and proton conductivity of the porous medium are corrected based on the volume fractions of electrical conductive material, $\varepsilon_{\mathrm{ele}}$, and ionomer, $\varepsilon_{\mathrm{ion}}$, respectively so that (Bruggeman correction):

$$\sigma_{\mathrm{ele}}^{\mathrm{eff}} = \varepsilon_{\mathrm{ele}}^{1.5} \sigma_{\mathrm{ele}} \quad [7]$$

$$\sigma_{\mathrm{ion}}^{\mathrm{eff}} = \varepsilon_{1}^{1.5} \sigma_{\mathrm{ion}} \quad [8]$$

Proton conductivities of membrane and ionomer in the catalyst layers are strongly related to water content. Relation of membrane water and proton conductivity was given by Ref. 31

$$\sigma_{\mathrm{ion}} = (0.5139\lambda - 0.326) \exp\left[2222\left(\frac{1}{303.15} - \frac{1\mathrm{K}}{T}\right)\right] \mathrm{S\ m^{-1}} \quad [9]$$

Source terms in the Eqs. 5 and 6 are the local reaction rates expressing in current in catalyst layer, while source terms in membrane, GDL, BP equal to zero.

$$S_{\mathrm{ion}} = -S_{\mathrm{ele}} = j \quad [10]$$

Gas species transport.—The conservation law for total mass and gas species are written as

$$\frac{\partial}{\partial t}(\varepsilon_{\mathrm{eff}} \rho) + \nabla \cdot (\rho \vec{u}) = S_{\mathrm{m}} \quad [11]$$

$$\varepsilon_{\mathrm{eff}} \rho \frac{\partial \omega_i}{\partial t} + \nabla \cdot \vec{j}_i + \rho(\vec{u} \cdot \nabla)\omega_i = S_i,\ \ i = \mathrm{H_2,\ O_2,\ N_2,\ H_2O} \quad [12]$$

where diffusion is described by Maxwell-Stefan Equation.

$$\vec{j}_i = -\rho \omega_i \sum_k \tilde{D}^{\mathrm{eff}}{}_{ik} \vec{d}_k \quad [13]$$

$$\vec{d}_k = \nabla x_k + \frac{1}{p}[(x_k - \omega_k)\nabla p] \quad [14]$$

and convection is described by Darcy's Law

$$\vec{u} = -\frac{\kappa}{\mu} \nabla p \quad [15]$$

Here, ω_i is the mass fraction of species i and $\varepsilon_{\mathrm{eff}}$ is the effective porosity expressed as $\varepsilon_{\mathrm{eff}} = (1 - s_{\mathrm{ice}})\varepsilon$ considering the influence of ice through the ice fraction s_{ice}. In Eq. 15, $\vec{u}$ is the gas velocity, κ is permeability and μ is dynamic viscosity.

The Bruggeman correction is used to describe the influence of porous medium and ice on gas transport as

$$\tilde{D}^{\mathrm{eff}}{}_{ik} = \varepsilon_{\mathrm{eff}}^{1.5} \cdot \tilde{D}_{ik} \quad [16]$$

Properties of the mixture and molar fractions of species can be calculated from the total density and mass fraction of species, as

$$M_{\mathrm{n}} = \left(\sum_i \frac{\omega_i}{M_i}\right)^{-1},\ p = \frac{RT\rho}{M_{\mathrm{n}}},\ x_i = \frac{\omega_i}{M_i} M_{\mathrm{n}} \quad [17]$$

Source terms of different species in Eq. 12 include electrochemical reaction and phase change, listed in Table II. And the source term of total mass is $S_{\mathrm{m}} = \sum S_i$.

Water transport and phase change.—In normal temperature operation, water in the fuel cell exists as vapor, liquid water and membrane water. In membrane and catalyst layer, the ionomer consists of backbones flexible perfluorocarbons and hydrophilic clusters with $H^+SO_3^-$ which can be considered as dilute acids. Water in ionomer bounds with proton of $H^+SO_3^-$ and they move together.[51] During cold start and at subzero condition, water mainly exist as vapor, ice and membrane water. Supercooled water and frozen membrane water may also exist but they are not considered. The mass conservation equation of membrane water reads

$$\varepsilon \frac{\partial c_{\mathrm{mw}}}{\partial t} + \frac{\partial}{\partial x}\left(-D_{\mathrm{mw}}^{\mathrm{eff}} \frac{\partial c_{\mathrm{mw}}}{\partial x} + \frac{2.5}{22}\frac{I_{\mathrm{ion}}}{F}\frac{EW}{\rho_{\mathrm{mem}}} c_{\mathrm{mw}}\right) = S_{\mathrm{mw}} \quad [18]$$

Here, the ionomer volume fraction ε is equal to 1 in the membrane, and equal to ε_{l} in the CL. Moreover, c_{mw} is the membrane water concentration in ionomer phase, EW is the equivalent weight (the ratio of mass and mole of sulfonic acid group) and ρ_{mem} is the density of dry membrane. Water content in membrane is written with the number of water molecules per sulfonic acid group, defined as

$$\lambda = \frac{c_{\mathrm{mw}} EW}{\rho_{\mathrm{mem}}} \quad [19]$$

The diffusion coefficient is related to membrane water content and temperature, and can be determined experimentally.[52] It is also corrected in CL using ionomer fraction via Bruggeman correlation, as

$$D_{\mathrm{mw}} = \begin{cases} 3.1 \times 10^{-7}\lambda[\exp(0.28\lambda) - 1]\exp\left(-\frac{2346}{T}\right), & \lambda \leqslant 3 \\ 4.17 \times 10^{-8}\lambda[1 + 161\exp(-\lambda)]\exp\left(-\frac{2346}{T}\right), & \lambda > 3 \end{cases} \quad [20]$$

$$D_{\mathrm{mw}}^{\mathrm{eff}} = \varepsilon^{1.5} D_{\mathrm{mw}} \quad [21]$$

Since water bonds with proton in membrane, moving of proton (current in ionomer) will cause extra moving force of water, i.e. electro osmotic drag. The electro osmotic drag is linear with water content and current. Noted that the current in ionomer varies with location in CL because of the current source from reaction.

Membrane water is produced in the cathode catalyst layer from reaction as well as from phase change of vapor and ice, so that the source term of membrane water can be expressed as.

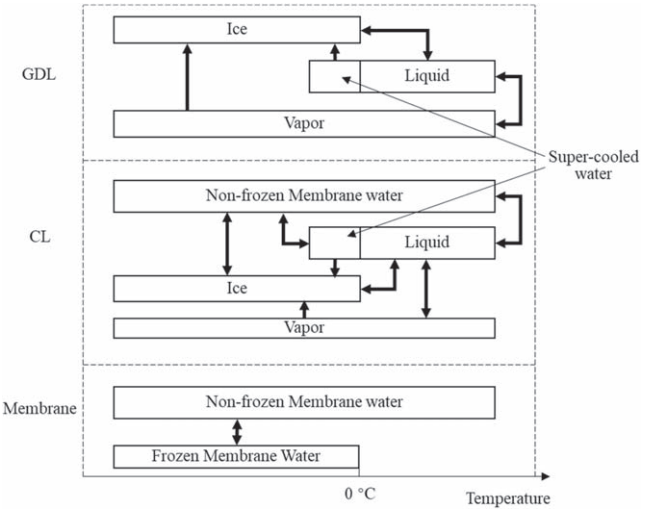

Figure 2. Schematics of water states and phase change in fuel cell.

$$S_{\mathrm{mw}} = \begin{cases} -S_{\mathrm{m\text{-}i}} - S_{\mathrm{m\text{-}v}}, & \mathrm{ACL} \\ 0, & \mathrm{PEM} \\ -S_{\mathrm{m\text{-}i}} - S_{\mathrm{m\text{-}v}} - M_{\mathrm{O_2}} j/2F, & \mathrm{CCL} \end{cases} \quad [22]$$

Note that the source term vanishes in the membrane.

According to Ref. 32 and recent studies on super-cooled water,[17,20–22] water existing states and phase change relationship in different layers and at different temperature are shown in Fig. 2. Super-cooled water is more likely to exist at temperature close to zero, or at above −10 °C, and its behavior is stochastic.[17] This study focuses on fuel cell cold start from a relatively low temperature, such as −20 °C. So super-cooled water is not included in this study.

A non-equilibrium phase change model is used, and phase change relationship of different forms of water in fuel cell at sub-zero temperature, as shown in Fig. 2. Phase change rates are calculated referring to Ref. 32 with predefined membrane water to vapor phase change coefficients $\gamma_{\mathrm{m\text{-}v}}$, membrane water to ice change coefficients $\gamma_{\mathrm{m\text{-}i}}$ and vapor to ice phase change coefficients $\gamma_{\mathrm{v\text{-}i}}$.

Phase change rate from membrane water to vapor is assumed to be linear with difference between membrane water content and equivalent water content of vapor and surface area (linear to ice volume fraction), written as

$$S_{\mathrm{m\text{-}v}} = \gamma_{\mathrm{m\text{-}v}}(1 - s_{\mathrm{ice}})\frac{\rho_{\mathrm{m}}}{EW}\left(\lambda - \lambda_{\mathrm{eq}}\left(\frac{c_{\mathrm{vap}}}{c_{\mathrm{sat}}}\right)\right) \quad [23]$$

where s_{ice} is ice volume fraction in the pore, also named as ice saturation. According to Zawodzinski et al.'s experiment,[53] there is a relationship of water content λ vs water vapor activity a_{w}[54] at equilibrium state. This relationship was further studied by Hinatsu et al. [55] and smoothed by Bao et al.,[56] which is used in the cold start model, as

Table II. Source terms of gas species.

Gas species	ACL	CCL	GDL
H_2	$S_{\mathrm{H_2}} = -\frac{M_{\mathrm{H_2}} j}{2F}$	0	0
O_2	0	$S_{\mathrm{O_2}} = -\frac{M_{\mathrm{O_2}} j}{4F}$	0
H_2O	$S_{\mathrm{H_2O}} = S_{\mathrm{m-v}} - S_{\mathrm{v-i}}$	$S_{\mathrm{H_2O}} = S_{\mathrm{m-v}} - S_{\mathrm{v-i}} - \frac{M_{\mathrm{O_2}} j}{2F}$	$S_{\mathrm{H_2O}} = -S_{\mathrm{v-i}}$
N_2	0	0	0

$$\lambda = \frac{1}{2}(0.043 + 17.81a_w - 39.85a_w^2 + 36.0a_w^3) \times (1 - \tanh(100(a_w - 1))) + \frac{1}{2}(14 + 8(1 - \exp(-s(a_w - 1)))) \times (1 + \tanh(100(a_w - 1))) \quad [24]$$

$$a_w = \frac{c_{vap}}{c_{sat}} \quad [25]$$

Saturation value of vapor c_{sat} depends on temperature T in Kelvin in Eq. 26.

$$\log_{10}\left(\frac{RTc_{sat}}{p_{atm}}\right) = -2.1794 + 0.02953 \times (T - 273.15) - 9.1837 \times 10^{-5} \times (T - 273.15)^2 + 1.4454 \times 10^{-7} \times (T - 273.15)^3 \quad [26]$$

Phase change rate from membrane water to ice is assumed to be linear to saturation of membrane water and surface area (linear to ice volume fraction). Since the freezing-point depression of water in the cathode CL is never greater than 2 °C and plays a negligible role,[16] 273.15 K is used as freezing-point T_F, so that

$$S_{m\text{-}i} = \begin{cases} \gamma_{m\text{-}i}(1 - s_{ice})\frac{\rho_m}{EW}(\lambda - \lambda_{sat}(T)), & \text{if } \lambda > \lambda_{sat}(T) \text{ and } T < T_F \\ 0, & \text{others} \end{cases} \quad [27]$$

The saturation value of membrane water at different temperatures is determined by Thompson et al. through differential scanning calorimetry (DSC)[57] and fitted by Jiao et al.[32] as

$$\lambda_{sat} \begin{cases} = 4.837, & \text{if } T < 223.15 \text{ K} \\ = \left[-1.304 + 0.01479T - 3.594 \times 10^{-5}T^2 \right]^{-1}, & \text{if } 223.15 \text{ K} \leqslant T < T_F \\ > \lambda, & \text{if } T \geqslant T_F \end{cases} \quad [28]$$

With the source of ice from membrane water, the ice mass conservation equation reads

$$\varepsilon \frac{\rho_{ice}}{M_{H_2O}} \frac{\partial s_{ice}}{\partial t} = S_{m\text{-}i} + S_{v\text{-}i} \quad [29]$$

where s_{ice} is the ice volume fraction in the pore, ε is the porosity of CL or GDL and ρ_{ice} is the density of ice Moreover, $S_{v\text{-}i}$ is the molar source term from vapor to ice. Since the phase change between ice and vapor is slow at vapor unsaturated state. So in this model, phase change rate from vapor to ice is assumed to be linear to degree of super saturation of vapor and porosity when the temperature is lower than freezing point and vapor concentration is higher than saturation value. In other conditions, phase change from ice to vapor is neglected.

$$S_{v\text{-}i} = \begin{cases} \gamma_{v\text{-}i}(1 - s_{ice})\varepsilon_{cl}(c_{vap} - c_{sat}), & \text{if } T < T_F \text{ and } c_{vap} > c_{sat} \\ 0, & \text{others} \end{cases} \quad [30]$$

Heat transfer.—The conservation of energy in the whole computation domain is

$$(\rho c_p)_{eff}\frac{\partial}{\partial t}T + \nabla \cdot (-k_{eff}\nabla T) = S_{heat} \quad [31]$$

where $(\rho c_p)_{eff}$ and k_{eff} are effective volumetric heat capacity and conductivity, calculated based on properties of ionomer and solid electron conductive material. To simplify our calculations, influence of gas species and ice on heat transfer is neglected, so that

$$(\rho c_p)_{eff} = \omega\rho_m c_{p,m} + (1 - \varepsilon - s_{ion})\rho_s c_{p,s} \quad [32]$$

$$k_{eff} = s_{ion}k_m + (1 - \varepsilon - s_{ion})k_s \quad [33]$$

Here, s_{ion} is the volume fraction of ionomer and $(1 - \varepsilon - s_{ion})$ is the volume fraction of solid electron conductive material. Thermal properties of part of BP with gas channel or coolant channel are also corrected according to the geometry, as

$$(\rho c_p)_{eff} = \begin{cases} \rho_{bp}c_{p,bp} \cdot \frac{W_{rib}}{W_{rib} + W_{gc}}, & \text{BP with gas channel} \\ \rho_{bp}c_{p,bp} \cdot \frac{W_{c,rib}}{W_{c,rib} + W_{cc}} + \rho_c c_c \cdot \frac{W_{cc}}{W_{c,rib} + W_{cc}}, & \text{BP with coolant channel} \end{cases} \quad [34]$$

$$k_{eff} = \begin{cases} k_{bp} \cdot \frac{W_{rib}}{W_{rib} + W_{gc}}, & \text{BP with gas channel} \\ k_{bp} \cdot \frac{W_{c,rib}}{W_{c,rib} + W_{cc}} + k_c \cdot \frac{W_{cc}}{W_{c,rib} + W_{cc}}, & \text{BP with coolant channel} \end{cases} \quad [35]$$

The different heat source terms are shown in Table III. These include Joule heating in all zones of the cell, and heat of reaction, in the CCL. Note that the heat of reaction in CCL consists of reversible heat $j\frac{T\Delta S}{2F}$ and irreversible heat $|\eta j|$ due to overpotential, where $\Delta S = -163.11\ \text{J mol}^{-1}\ \text{K}^{-1}$ is the entropy change of the reaction.

Phase change heat can be calculated based on phase rate of water. According to Thompson et al.,[57] membrane water has similar enthalpy and can be assumed to be liquid state when calculating phase change heat, so that

Table III. Heat source terms for Eq. 31.

	Reaction heat	Joule	Phase change heat
PEM	0	$\sigma_{ion}^{eff}(\nabla\phi_{ion})^2$	0
ACL	0	$\sigma_{ele}^{eff}(\nabla\phi_{ele})^2 + \sigma_{ion}^{eff}(\nabla\phi_{ion})^2$	S_{pc}
CCL	$-j\frac{T\Delta S}{2F} + \lvert\eta j\rvert$	$\sigma_{ele}^{eff}(\nabla\phi_{ele})^2 + \sigma_{ion}^{eff}(\nabla\phi_{ion})^2$	S_{pc}
GDL	0	$\sigma_{ele}^{eff}(\nabla\phi_{ele})^2$	S_{pc}
BP	0	$\sigma_{ele}^{eff}(\nabla\phi_{ele})^2$	0

$$S_{\text{pc}} = -\Delta h_{\text{evap}} S_{\text{m-v}} + (\Delta h_{\text{evap}} + \Delta h_{\text{fusion}}) S_{\text{v-i}} + \Delta h_{\text{fusion}} S_{\text{m-i}} \quad [36]$$

Here, Δh_{evap} is the latent heat of evaporation and Δh_{fusion} is latent heat of fusion.

Boundary and initial conditions.—Conservation equations are presented in 2.1–2.4. For charge conservation, anode BP boundary is set as potential ground and a constant current is drawn from the cell, the resulting potential at cathode BP boundary is the cell output voltage.

For gas species transport, a lumped gas channel model is used, as shown in Eq. 37. In anode $i = \text{H}_2, \text{H}_2\text{O}$ and in cathode $i = \text{O}_2, \text{N}_2, \text{H}_2\text{O}$.

$$\begin{cases} L_{\text{agc}} W_{\text{agc}} \dfrac{d}{dt} c_{\text{agc},i} = N_{\text{agc,in},i} - N_{\text{agc,out},i} - N_{\text{agc2agdl},i} \\ L_{\text{agc}} W_{\text{cgc}} \dfrac{d}{dt} c_{\text{cgc},i} = N_{\text{cgc,in},i} - N_{\text{cgc,out},i} - N_{\text{cgc2cgdl},i} \end{cases} \quad [37]$$

The fluxes in Eq. 37 are calculated as follows: Inlet gas molar fractions are calculated based on humidification condition, which is set to zero humidification in cold start. α_{H_2} and α_{O_2} are hydrogen and air stoichiometric ratios respectively. Coefficients $k_{\text{agc,out}}$ and $k_{\text{cgc,out}}$ in $\text{kg}/s/\text{Pa}$ are used to describe gas channel outlet condition.

$$\begin{cases} \mathbf{N}_{\text{agc,in,H}_2} = \alpha_{\text{H}_2} \dfrac{I_{\text{cell}} A}{2F}, \\ \mathbf{N}_{\text{agc,in,H}_2\text{O}} = \mathbf{N}_{\text{agc,in,H}_2} \dfrac{1 - x_{\text{agc,in,H}_2}}{x_{\text{agc,in,H}_2}} \quad \text{anode} \\ \mathbf{N}_{\text{cgc,in,O}_2} = \alpha_{\text{O}_2} \dfrac{I_{\text{cell}} A}{4F}, \\ \mathbf{N}_{\text{agc,in,N}_2} = \mathbf{N}_{\text{agc,in,O}_2} \dfrac{x_{\text{agc,in,N}_2}}{x_{\text{agc,in,O}_2}}, \\ \mathbf{N}_{\text{agc,in,H}_2\text{O}} = \mathbf{N}_{\text{agc,in,O}_2} \dfrac{x_{\text{agc,in,H}_2\text{O}}}{x_{\text{agc,in,O}_2}} \quad \text{cathode} \end{cases} \quad [38]$$

$$\begin{cases} \mathbf{N}_{\text{agc,out}} = \dfrac{k_{\text{agc,out}}}{M_{n,\text{agc}}} \left(RT \sum c_{\text{agc},i} - p_{\text{atm}} \right), \ \mathbf{N}_{\text{agc,out},i} = \mathbf{N}_{\text{agc,out}} x_i \\ \mathbf{N}_{\text{cgc,out}} = \dfrac{k_{\text{cgc,out}}}{M_{n,\text{cgc}}} \left(RT \sum c_{\text{cgc},i} - p_{\text{atm}} \right), \ \mathbf{N}_{\text{cgc,out},i} = \mathbf{N}_{\text{cgc,out}} x_i \end{cases} \quad [39]$$

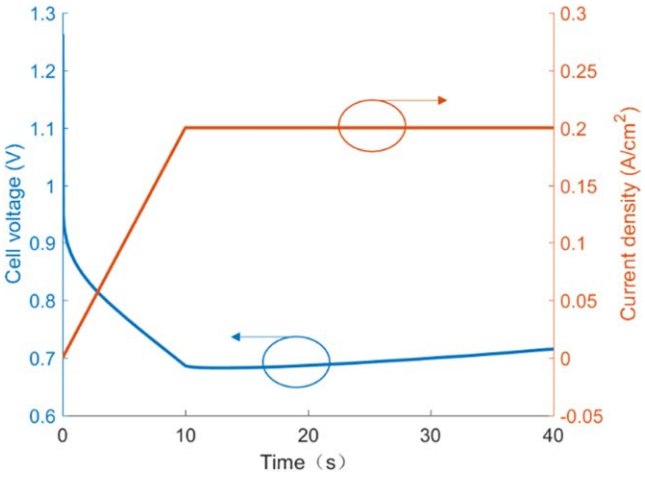

Figure 3. Variation of current density and cell voltage.

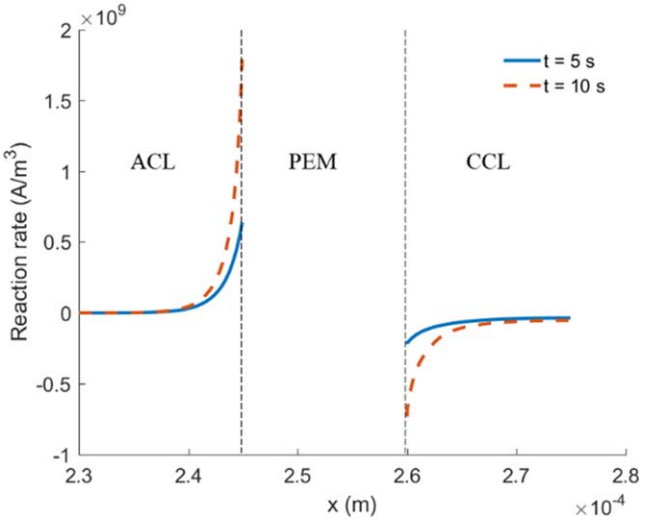

Figure 4. Distribution of reaction rate.

$$\begin{cases} \mathbf{N}_{\text{agc2agdl},i} = h(c_{i,\text{agc}} - c_i|_{\text{agdl-agc}}) \cdot L_{\text{gc}} W_{\text{agc}} \\ \mathbf{N}_{\text{cgc2cgdl},i} = h(c_{i,\text{cgc}} - c_i|_{\text{cgdl-cgc}}) \cdot L_{\text{gc}} W_{\text{cgc}} \end{cases} \quad [40]$$

Membrane boundary condition at the interface of CL and GDL is no flux boundary $\frac{\partial c_{\text{mw}}}{\partial x} = 0$, since there is no ionomer in GDL.

For heat transfer, the model is used to simulate the cell in the middle of the stack so a cyclic thermal boundary condition is used, i.e. the temperature and temperature gradient at left boundary of the single cell model are equal to those at right boundary of the model respectively. And the coolant is assumed to be still during the cold start.

The initial values of membrane water and temperature are set to uniform distribution, while the concentrations of the different gas species equal to inlet concentrations; Initial ice fraction is zero.

Simulation results.—Discretization and numerical simulation of the developed 1D model are conducted on COMSOL Multiphysics. Conservation equations Eqs. 5 are solved. The initial water content is $\lambda = 5$ and initial temperature is $T_0 = -20$ °C. The controlled current density is 0.2A cm^{-2}, ramping up from zero at a rate of $0.02\text{A}/(\text{cm}^2\text{s})$. Inlet gas temperature is -20 °C and the stoichiometric ratios are $\alpha_{\text{H}_2} = 1.2$ and $\alpha_{\text{O}_2} = 1.5$. For a cold start of 40 s duration, the computational time is 216 s on a laptop with i5–6300 HQ and 16 GB RAM.

Figure 3 shows the variation of current and cell voltage during the cold start. The voltage drops slowly due to the increase of current at the beginning, which leads to irreversible losses due to overpotential and ohmic loss. When the current stays constant, for t > 10 s, cell voltage slightly increases because the continuing hydration of the membrane and the increase of temperature, which both reduce losses.

The reaction rate in catalyst layer is not distributed evenly, as shown in Fig. 4. This is consistent with the existing literature about reaction rate distribution.[58,59] Reaction mainly takes place in near membrane part, because the proton transport resistance in ionomer is much higher than electron transport resistance in the electrical conductive material of the CL. From these observations one might conclude that a lumped CL model, where the CL is described by only one state, might not be suitable for accurate calculation of the reaction rate or overpotential.

Figure 5 shows the distribution of membrane water at different time. We can see that water content of membrane and CCL keeps increasing, while in the ACL it decreases during the first 20 s and then increases. This is because water is dragged from anode to cathode by the proton, i.e. electro osmotic drag. There are strong

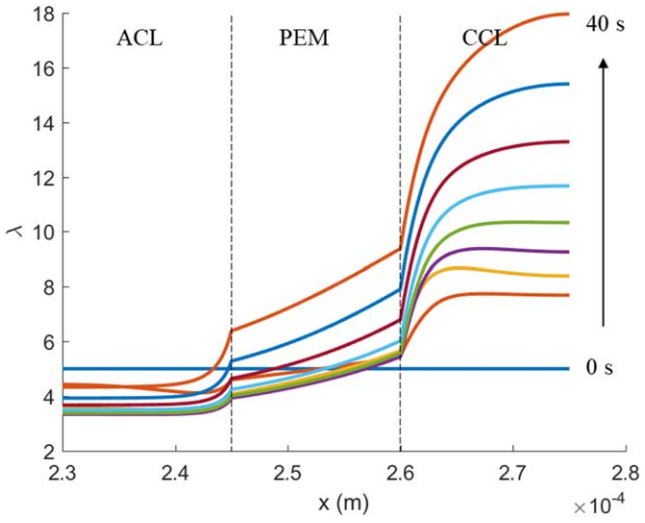

Figure 5. Distribution of membrane water content in λ.

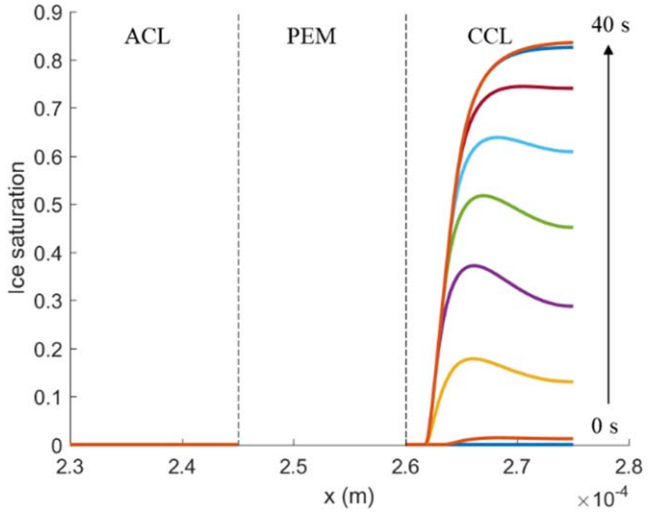

Figure 6. Distribution of ice volume fraction.

concentration gradients at the interface of ACL/PEM and PEM/CCL. Water content in membrane is almost linearly distributed.

Ice is only formed in the CCL, as shown in Fig. 6, where the main source of ice is phase change from membrane water. Closer to the membrane the water content in the CCL is relatively low and lies below the saturation value near membrane, hence there is no ice forming in this area.

Temperature distribution and its temporal variation are shown in Fig. 7a. The temperature peak locates in CCL because the main heat source is the ORR in CCL. Temperature difference in BP is small, owing to the high thermal conductivity of BP, which is graphite in this study. Details of the temperature distribution are shown in Fig. 7b. Temperature distribution in each functional layer is near linear, which indicates that a lumped temperature can approximate the temperature of the layer.

The results presented above show key features of cold start of fuel cell. The temperature distribution is basically linear, while distribution of reaction rate, membrane water and ice volume fraction are strongly nonuniform in CL. Especially, distributions in CL near membrane are significantly different from that near GDL.

Model Simplification

Although one-dimensional model has significantly lower computational cost than a three dimensional model, it still does not suffice to integrate into a stack model, mainly due to the complex multi-physics in CL. In Zhou et al.'s stack model, the charge conservation equations (Eqs. 5 and 6) were not solved.[43] Instead, a lumped overpotential and reaction rate model was used in order to reduce the computational cost. However, from the results presented in the literature and the model developed in this paper, the distributions of reaction rate, membrane water and ice fraction are strongly nonuniform. The following simplifications of the cold start model focuses on keeping these distribution features, while simplifying the model, so that calculations are fast.

Definition of different regions of the cells is shown in Fig. 8, in which the single cell is divided into twelve regions. Both anode and cathode catalyst layers are divided into two regions to describe the nonuniformity in CL. In this section, the variables in region i will be marked with a subscript i, and variables at the interface of region i and j will be marked with a subscript $i-j$. For the average value of ACL (Region 4 and 5) or CCL (region 7 and 8), acl or ccl will be used as subscripts.

Gas transport.—According to the simulation results of the 1D model, gas transport is much faster than membrane water transport

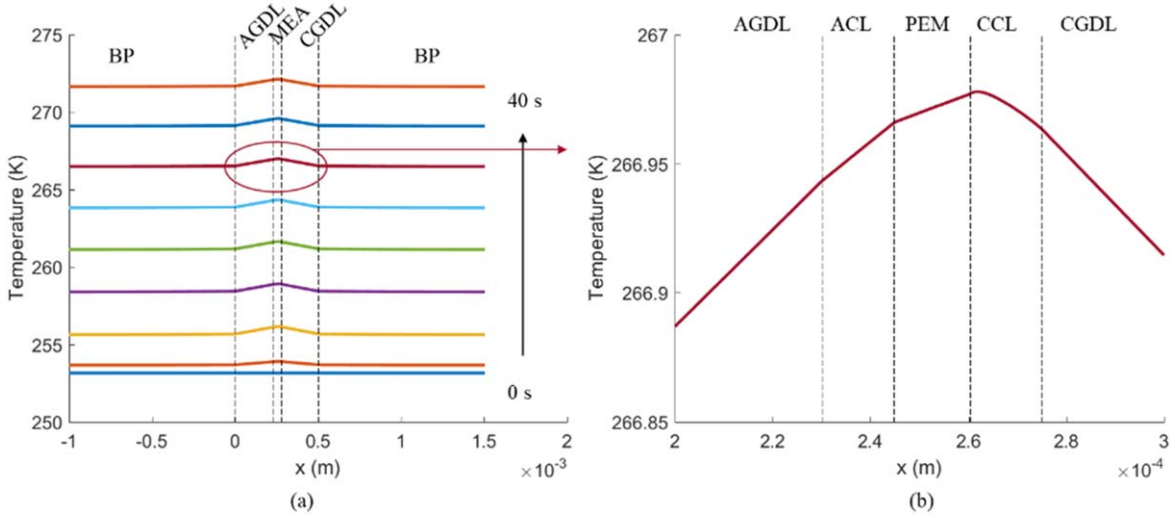

Figure 7. Temperature distribution during cold start: (a) in the whole cell, (b) in MEA at 30 s.

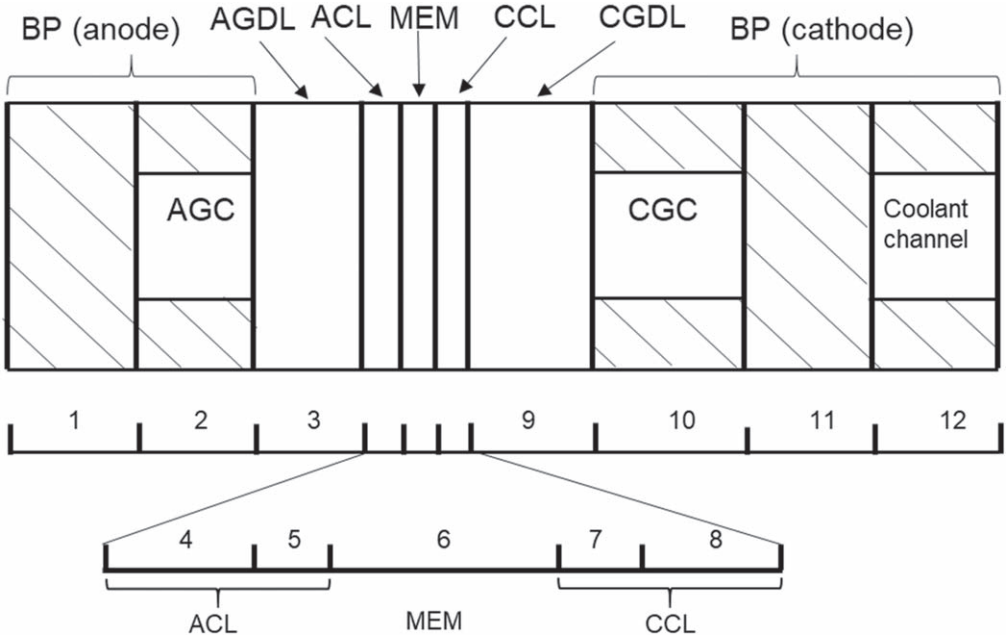

Figure 8. Regions definition of simplified model.

and diffusion dominates in both anode and cathode. Thus, several assumptions are used in the simplification of gas transport:

(1) Steady state gas diffusion model is used, so that

$$J_{O_2,9-10} = J_{O_2,8-9} = \frac{I_{cell}}{4F} \quad [41]$$

$$J_{H_2O,2-3} = J_{H_2O,3-4} = J_{H_2O,a} \quad [42]$$

$$J_{H_2O,9-10} = J_{H_2O,8-9} = J_{H_2O,c} \quad [43]$$

(2) Pressures in GDL and CL are assumed to be equal to pressures in gas channels. Hence, only water vapor concentration is calculated at the anode, and oxygen and water vapor are calculated in cathode.
(3) Constant diffusion coefficients in porous media and boundary of GDL/GC are used.

Using the current density, oxygen concentration in gas channel and the transport coefficients, oxygen concentration at different interface can be obtained as,

$$\frac{i_{cell}}{4F} = h_{O_2,9-10}(c_{10}^{O_2} - c_{9-10}^{O_2}) = D_{O_2,9}^{eff}(c_{9-10}^{O_2} - c_{8-9}^{O_2}) = D_{O_2,ccl}^{eff}(c_{8-9}^{O_2} - c_{ccl}^{O_2}) \quad [44]$$

where $h_{O_2,9-10}$, $D_{O_2,9}^{eff}$, $D_{O_2,ccl}^{eff}$ are transport coefficients at CGC/CGDL interface, inside CGDL and CCL.

As for water phase change and transport of water vapor, water content in CL and vapor concentration in gas channel are used to determine the vapor flux. Water vapor concentration in CL is approximately considered to be equal to concentration at the CL/GDL interface.

$$J_{H_2O,c} = \gamma\varepsilon_{cl}\beta H_{electrode}\frac{\rho_{mem}}{M_{mem}}(\lambda_{eq,7-8} - \lambda_7) + \gamma\varepsilon_{cl}(1-\beta)H_{electrode}\frac{\rho_{mem}}{M_{mem}}(\lambda_{eq,7-8} - \lambda_8) = D_{H_2O,9}^{eff}(c_{9-10}^{H_2O} - c_{8-9}^{H_2O}) = h_{v,9-10}(c_{10}^{H_2O} - c_{9-10}^{H_2O}) \quad [45]$$

Equation 24 shows the equilibrium relation of membrane water and vapor concentration. The equilibrium vapor concentration of membrane water content $c_{eq}(\lambda)$ in CL can be calculated based on this relationship. The phase change rate between membrane water and water vapor is fast so phase change can be written as follows. Water vapor flux in cathode and concentration at CGDL/CGC interface can be determined from

$$J_{H_2O,c} = \gamma_{m\text{-}v}\varepsilon_{cl}\beta\delta_{cl}\frac{\rho_{mem}}{EW}\frac{\partial\lambda}{\partial c}\bigg|_{\lambda=\lambda_7}(c_{8-9}^{H_2O} - c_{eq}(\lambda_7)) + \gamma_{m\text{-}v}\varepsilon_{cl}(1-\beta)\delta_{cl}\frac{\rho_{mem}}{EW}\frac{\partial\lambda}{\partial c}\bigg|_{\lambda=\lambda_8}(c_{8-9}^{H_2O} - c_{eq}(\lambda_8)) \quad [46]$$

Anode water flux and concentration are also obtained through the same method, using Eq. 47.

$$J_{H_2O,a} = \gamma_{m\text{-}v}\varepsilon_{cl}(1-\beta)\delta_{cl}\frac{\rho_{mem}}{EW}\frac{\partial\lambda}{\partial c}\bigg|_{\lambda=\lambda_4}(c_{3-4}^{H_2O} - c_{eq}(\lambda_4)) + \gamma_{m\text{-}v}\varepsilon_{cl}\beta\delta_{cl}\frac{\rho_{mem}}{EW}\frac{\partial\lambda}{\partial c}\bigg|_{\lambda=\lambda_5}(c_{3-4}^{H_2O} - c_{eq}(\lambda_5)) = D_{H_2O,3}^{eff}(c_{2-3}^{H_2O} - c_{3-4}^{H_2O}) = h_{v,2-3}(c_2^{H_2O} - c_{2-3}^{H_2O}) \quad [47]$$

Transport coefficients are listed in Table IV.

Membrane water.—Since there is strong nonuniformity of membrane water distribution in CL, a five-region model of membrane water in MEA is developed, as shown in Fig. 9. Membrane water in CL near GDL is considered as uniform distribution, while water in CL near membrane is assumed to distribute linearly and water in membrane is two segment linear distribution. β is the proportion of the part closer to the membrane, and it is set as 0.3, which is also used in electrochemical reaction in 3.3.

In Fig. 9, c_4, c_5, c_6, c_7 and c_8 are independent variables. Mass conservation of membrane water reads

Table IV. Parameters of simplified model.

Parameter	Value
Diffusivities of oxygen	$D_{O_2} = 2.652 \times 10^{-5} \times (T/333.15\text{K})^{1.5}\text{m}^2 \cdot \text{s}^{-1}$
Diffusivities of vapor in anode	$D_{v,a} = 5.457 \times 10^{-5} \times (T/333.15\text{K})^{1.5}\text{m}^2 \cdot \text{s}^{-1}$
Diffusivities of vapor in cathode	$D_{v,c} = 2.236 \times 10^{-5} \times (T/333.15\text{K})^{1.5}\text{m}^2 \cdot \text{s}^{-1}$

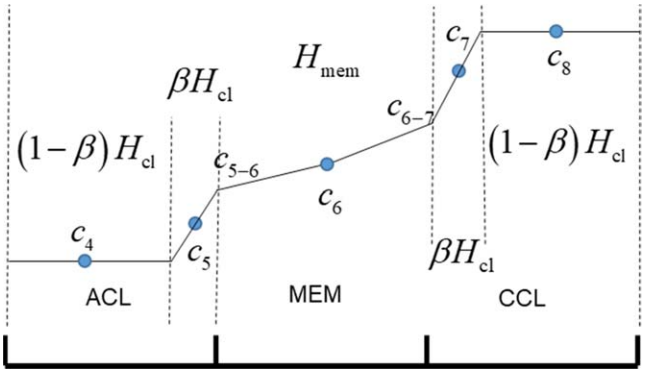

Figure 9. Five-region membrane water model in MEA.

$$\begin{cases} s_{\text{ion}}(1-\beta)\delta_{\text{cl}}\dfrac{\text{d}c_4}{\text{d}t} = -J^{\text{d}}_{4-5} - J^{\text{e}}_{4-5} + S_{\text{mw},4} \\ s_{\text{ion}}\beta\delta_{\text{cl}}\dfrac{\text{d}c_5}{\text{d}t} = J^{\text{d}}_{4-5} + J^{\text{e}}_{4-5} - J^{\text{d}}_{5-6} - J^{\text{e}}_{5-6} + S_{\text{mw},5} \\ \delta_{\text{mem}}\dfrac{\text{d}c_6}{\text{d}t} = J^{\text{d}}_{5-6} + J^{\text{e}}_{5-6} - J^{\text{d}}_{6-7} - J^{\text{e}}_{6-7} \\ s_{\text{ion}}\beta\delta_{\text{cl}}\dfrac{\text{d}c_7}{\text{d}t} = J^{\text{d}}_{6-7} + J^{\text{e}}_{6-7} - J^{\text{d}}_{7-8} - J^{\text{e}}_{7-8} + S_{\text{mw},7} \\ s_{\text{ion}}(1-\beta)\delta_{\text{cl}}\dfrac{\text{d}c_8}{\text{d}t} = J^{\text{d}}_{7-8} + J^{\text{e}}_{7-8} + S_{\text{mw},8} \end{cases} \quad [48]$$

Where J^{d}_{i-j} and J^{e}_{i-j} are the diffusion flux and electro osmotic drag from c_i to c_j respectively.

There is a change of concentration gradient at the interface of membrane and CL because of the discontinuity of ionomer fraction. At the interface of CL/PEM, the relation of fluxes is:

$$\begin{cases} J^{\text{d}}_{5-6} = s^{1.5}_{\text{ion}}D(c_{5-6})\theta_{\text{acl}}\dfrac{c_5 - c_{5-6}}{0.5\beta H_{\text{cl}}} = D(c_{5-6})\dfrac{c_{5-6} - c_6}{0.5H_{\text{mem}}} \\ J^{\text{e}}_{5-6} = \dfrac{2.5}{22}\dfrac{I_{\text{fc}}}{F}\dfrac{EW}{\rho_{\text{mem}}}c_{5-6} \end{cases} \quad [49]$$

$$\begin{cases} J^{\text{d}}_{6-7} = D(c_{6-7})\dfrac{c_6 - c_{6-7}}{0.5\delta_{\text{mem}}} = s^{1.5}_{\text{ion}}D(c_{6-7})\theta_{\text{ccl}}\dfrac{c_{6-7} - c_7}{0.5\beta\delta_{\text{cl}}} \\ J^{\text{e}}_{6-7} = \dfrac{2.5}{22}\dfrac{I_{\text{fc}}}{F}\dfrac{EW}{\rho_{\text{mem}}}c_{6-7} \end{cases} \quad [50]$$

where θ_{acl} and θ_{ccl} are correction factors as the real distribution of membrane water is not exactly linear. So we can calculate c_{5-6} from c_5 and c_6, and also calculate c_{6-7} from c_6 and c_7,

$$c_{5-6} = \frac{\frac{s^{1.5}_{\text{ion}}c_5}{0.5\beta\delta_{\text{cl}}} + \frac{c_6}{0.5\delta_{\text{mem}}}}{\frac{s^{1.5}_{\text{ion}}}{0.5\beta\delta_{\text{cl}}} + \frac{1}{0.5\delta_{\text{mem}}}}, \quad c_{6-7} = \frac{\frac{s^{1.5}_{\text{ion}}c_7}{0.5\beta\delta_{\text{cl}}} + \frac{c_6}{0.5\delta_{\text{mem}}}}{\frac{s^{1.5}_{\text{ion}}}{0.5\beta\delta_{\text{cl}}} + \frac{1}{0.5\delta_{\text{mem}}}} \quad [51]$$

The water concentration at the interface c_{5-6} and c_{6-7} are used to calculate the transport coefficients. Other fluxes are calculated using the water concentration difference, as

$$\begin{cases} J^{\text{d}}_{4-5} = s^{1.5}_{\text{ion}}D(c_4)\dfrac{c_4 - c_5}{0.5\delta_{\text{cl}}} \\ J^{\text{e}}_{4-5} = 0 \end{cases} \quad [52]$$

$$\begin{cases} J^{\text{d}}_{7-8} = s^{1.5}_{\text{ion}}D(c_8)\dfrac{c_7 - c_8}{0.5\delta_{\text{cl}}} \\ J^{\text{e}}_{7-8} = \dfrac{2.5}{22}\dfrac{I_2}{F}\dfrac{EW}{\rho_{\text{mem}}}c_8 \end{cases} \quad [53]$$

Reaction in anode is assumed to take place in the part of ACL close to PEM. In CCL, I_1 and I_2 stand for reaction rate in the two parts of CCL, which is further described and shown in 3.2.

Electrochemical reaction and charge transport.—Since the HOR in anode is much faster than the ORR in cathode, and the overpotential is also much lower in anode, the anode overpotential is neglected. In order to describe the reaction rate distribution, reaction in CCL is calculated in two parts in CCL, as shown in Fig. 10.

Equilibrium potential is calculated by (4) using the oxygen concentration in CCL. The following equations are solved to obtain the reaction rates and voltage loss in CCL:

$$\begin{cases} I_7 = \beta\delta_{\text{cl}}(1 - s_{\text{ice},7})\delta_{\text{cl}}j_{0,\text{c}}\dfrac{c_{\text{O}_2,\text{ccl}}}{c_{\text{O}_2,\text{ref}}} \\ \qquad \times\left[\exp\left(-\dfrac{F}{RT_{\text{ccl}}}(\phi_{e,7} - \phi_{i,7} - E_{\text{eq},7})\right)\right] \\ I_8 = (1-\beta)\delta_{\text{cl}}(1 - s_{\text{ice},8})\delta_{\text{cl}}j_{0,\text{c}}\dfrac{c_{\text{O}_2,\text{ccl}}}{c_{\text{O}_2,\text{ref}}} \\ \qquad \times\left[\exp\left(-\dfrac{F}{RT_{\text{ccl}}}(\phi_{e,8} - \phi_{i,8} - E_{\text{eq},8})\right)\right] \\ I_7 = \dfrac{\sigma^{\text{eff}}_{\text{ele,cl}}(\phi_{e,7} - \phi_{e,8})}{0.5\delta_{\text{cl}}} \\ I_8 = \dfrac{s^{1.5}_{\text{ion}}\sigma(c_8)(\phi_{i,7} - \phi_{i,8})}{0.5\delta_{\text{cl}}} \\ I_7 + I_8 = I_{\text{cell}} \end{cases} \quad [54]$$

Resistance of ACL, CCL are calculated as sums of ionic resistance and electric resistance, as

$$R_{\text{acl}} = \frac{(1-\beta)\delta_{\text{cl}}}{(1 - \varepsilon_{\text{cl}} - s_{\text{ion}})^{1.5}\sigma_{\text{ele,cl}}} + \frac{1}{3}\frac{\beta\delta_{\text{cl}}}{s^{1.5}_{\text{ion}}\sigma(c_{5-6})} \quad [55]$$

$$R_{\text{ccl}} = \frac{1}{2}\frac{\beta\delta_{\text{cl}}}{s^{1.5}_{\text{ion}}\sigma(c_{6-7})} + \frac{1}{2}\frac{(1-\beta)\delta_{\text{cl}}}{(1 - \varepsilon_{\text{cl}} - s_{\text{ion}})^{1.5}\sigma_{\text{ele,cl}}} \quad [56]$$

Referring to Ref. 47, two linear distributions of membrane water are used to calculate proton conductivity and then integrate into membrane resistance as

$$R_{\mathrm{m}} = \frac{\delta_{\mathrm{mem}}}{2\exp[1268(1/303.15 - 2/(T_{\mathrm{acl}} + T_6))]} \times \frac{\ln(0.51399\lambda_{5-6} - 0.326) - \ln(0.5139\lambda_6 - 0.326)}{0.5139(\lambda_{5-6} - \lambda_6)} + \frac{\delta_{\mathrm{mem}}}{2\exp[1268(1/303.15 - 2/(T_6 + T_{\mathrm{ccl}}))]} \times \frac{\ln(0.51399\lambda_6 - 0.326) - \ln(0.5139\lambda_{6-7} - 0.326)}{0.5139(\lambda_6 - \lambda_{6-7})} \quad [57]$$

$\sigma(c)$ is the proton conductivity of ionomer as a function of membrane water content c, developed by Springer et al.[54] as

$$\sigma_{\mathrm{m}} = \left(0.5139c\frac{EW}{\rho_{\mathrm{m}}} - 0.326\right)\exp[1268(1/303.15 - 1/T)] \quad [58]$$

Cell voltage is then obtained as

$$V_{\mathrm{cell}} = \phi_{\mathrm{e},8} - \phi_{\mathrm{i},7} - I_{\mathrm{cell}}\left(R_{\mathrm{acl}} + R_{\mathrm{ccl}} + R_{\mathrm{m}} + \frac{2\delta_{\mathrm{gdl}}}{(1-\varepsilon_{\mathrm{gdl}})^{1.5}\sigma_{\mathrm{ele,gdl}}} + \delta_{\mathrm{bp}}\sigma_{\mathrm{ele,bp}}\right) \quad [59]$$

Heat transport.—Temperature distribution is near linear in the results of 1D model. Ten lumped volumes are selected and the temperatures are calculated from the discrete heat equation

$$c_{p,i}\frac{\mathrm{d}T_i}{\mathrm{d}t} = k_{i,i-1}(T_{i-1} - T_i) + k_{i,i+1}(T_{i+1} - T_i) + S_{\mathrm{heat},i} \quad [60]$$

where C_i is thermal capacity and Q_i is heat source, and the conductivities $\kappa_{i,i-1}$ and $\kappa_{i,i+1}$ are calculated from thermal conductivities k_i and thickness H_i of different layers as

$$\kappa_{i,i+1} = \frac{1}{\frac{\delta_i}{2k_i} + \frac{\delta_{i+1}}{2k_{i+1}}} \quad [61]$$

Ohmic heat in BP is neglected, the other heat sources are calculated as

$$\begin{cases} S_{\mathrm{heat,gdl}} = \dfrac{I_{\mathrm{cell}}^2 H_{\mathrm{gdl}}}{\sigma_{\mathrm{ele,gdl}}^{\mathrm{eff}}} \\ S_{\mathrm{heat,acl}} = I_{\mathrm{cell}}^2 R_{\mathrm{acl}} - \Delta h_{\mathrm{evap}} J_{\mathrm{H_2O,a}} \\ Q_{\mathrm{heat,pem}} = I_{\mathrm{cell}}^2 R_{\mathrm{mem}} \\ S_{\mathrm{heat,ccl}} = I_{\mathrm{cell}}^2 R_{\mathrm{ccl}} + I_7^2 \dfrac{0.5\delta_{\mathrm{cl}}}{\kappa_{\mathrm{ele,cl}}^{\mathrm{eff}}} \\ \qquad + I_8^2 \dfrac{0.5\delta_{\mathrm{cl}}}{\varepsilon_1^{1.5}\sigma(c_7)} \\ \qquad + |I_7(\phi_{\mathrm{e},7} - \phi_{\mathrm{i},7} - E_{\mathrm{eq},7})| \\ \qquad + |I_8(\phi_{\mathrm{e},8} - \phi_{\mathrm{i},8} - E_{\mathrm{eq},8})| + \left| I_{\mathrm{cell}}\dfrac{T_{\mathrm{ccl}}\Delta S}{2F} \right| \\ \qquad - \Delta h_{\mathrm{evap}} M_{\mathrm{H_2O}} J_{\mathrm{H_2O,c}} + \Delta h_{\mathrm{fusion}} M_{\mathrm{H_2O}} J_{\mathrm{m2i}} \end{cases} \quad [62]$$

Ice formation.—According to the results of 1D model, ice formation is mainly from membrane water in CCL, so in this simplified model it is only considered in CCL. Similar to membrane water transport, ice volume fraction in the two regions of CCL, $s_{\mathrm{ice},1}$ and $s_{\mathrm{ice},2}$, are calculated separately, as

$$\varepsilon_{\mathrm{cl}}\rho_{\mathrm{ice}}\frac{\mathrm{d}s_{\mathrm{ice},7}}{\mathrm{d}t} = \gamma_{\mathrm{m\text{-}i}}(1 - s_{\mathrm{ice},7})M_{\mathrm{H_2O}}\frac{\rho_{\mathrm{m}}}{EW}(\lambda_7 - \lambda_{\mathrm{sat}}(T_{\mathrm{ccl}})),$$
$$\text{if } \lambda_7 > \lambda_{\mathrm{sat}}(T_{\mathrm{ccl}}) \text{ and } T_{\mathrm{ccl}} < T_{\mathrm{F}} \quad [63]$$

$$\varepsilon_{\mathrm{cl}}\rho_{\mathrm{ice}}\frac{\mathrm{d}s_{\mathrm{ice},8}}{\mathrm{d}t} = \gamma_{\mathrm{m\text{-}i}}(1 - s_{\mathrm{ice},8})M_{\mathrm{H_2O}}\frac{\rho_{\mathrm{m}}}{EW}(\lambda_8 - \lambda_{\mathrm{sat}}(T_{\mathrm{ccl}})),$$
$$\text{if } \lambda_8 > \lambda_{\mathrm{sat}}(T_{\mathrm{ccl}}) \text{ and } T_{\mathrm{ccl}} < T_{\mathrm{F}} \quad [64]$$

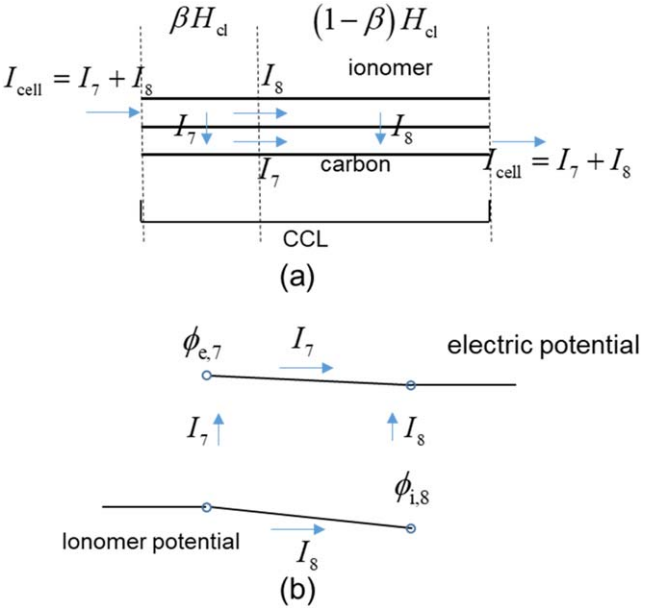

Figure 10. Reaction in CCL: (a) reaction rate and current, (b) potential and current.

Ice formation rate in CCL reads

$$J_{\mathrm{m2i}} = \gamma_{\mathrm{m\text{-}i}}(1 - s_{\mathrm{ice},7})\frac{\rho_{\mathrm{m}}}{EW}(\lambda_7 - \lambda_{\mathrm{sat}}(T_{\mathrm{ccl}})) + \gamma_{\mathrm{m\text{-}i}}(1 - s_{\mathrm{ice},8})\frac{\rho_{\mathrm{m}}}{EW}(\lambda_8 - \lambda_{\mathrm{sat}}(T_{\mathrm{ccl}})) \quad [65]$$

which contributes in heat source term in Eq. 62.

Comparison and discussion

Experimental validation.—In order to examine the accuracy of the presented 1D model and simplified model, cold start experiment

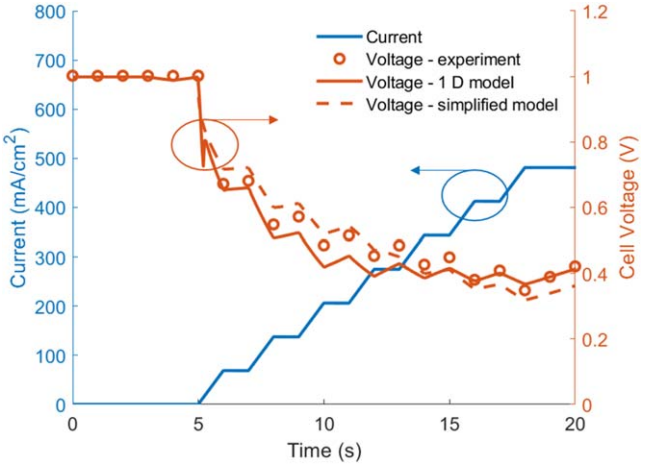

Figure 11. Experimental validation: cell voltage.

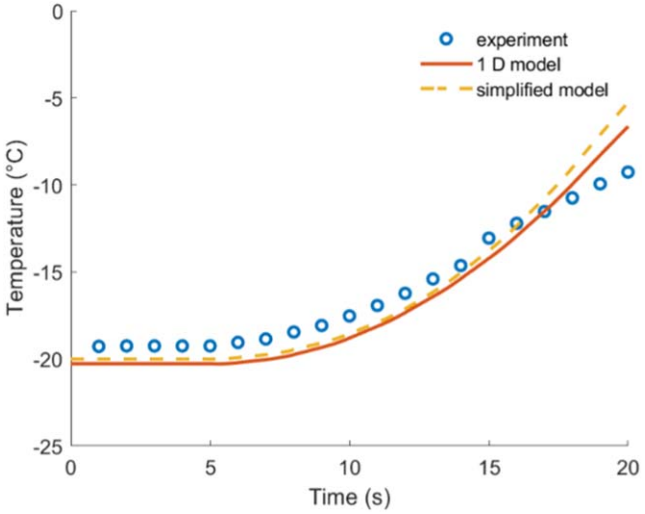

Figure 12. Experimental validation: Temperature in bipolar plate.

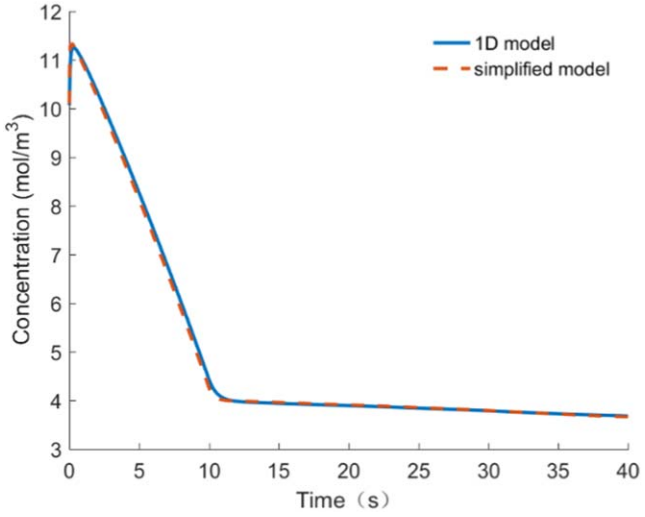

Figure 13. Comparison of oxygen concentration in CCL in 1D model and simplified model.

was conducted and compared with simulation results. Validation data was obtained from a fuel cell stack with 20 cells and an area of 291 cm^2 starting up from −20 °C. Cell 11, i.e. the cell in the middle of the stack, is analyzed, because it can represent the cell in a long stack during cold start. Four temperature sensors are install in the bipolar plate between Cell 10 and 11.

Before cold start experiment, the stack is purged with hydrogen at 30% relative humidity and dry air. The hydrogen and air stoichiometric ratios are 3 and 1.5 respectively. And the current density is Gradually increased to 500 mA cm^{-2}.

In order to keep the same operation conditions for experiment and model simulations, current density and reactant flow rate measured from experiment are used as input variables for the cold start model. According to the equilibrium membrane water from both anode and cathode side, initial membrane water content is set as $\lambda_0 = 1.6$ for both 1D model and simplified model. Both 1D model and simplified model are simulated using experiment condition.

Experimental validation results of the presented models are presented in Fig. 11 and Fig. 12, in which cell voltage and temperature in bipolar plate are compared respectively. The current density ramps up from zero to 500 mA cm^{-2} step by step, and the cell voltage drops from 1 V to near 0.3 V. Both 1D model and simplified model shows good accuracy at steady state points and the errors in dynamic loading process are larger. The overall errors of both 1D model and simplified model are within 15%. The temperature of bipolar plate increases gradually at the beginning. With the increase of current density and voltage loss, heat generation increases rapidly so that the temperature rises faster. The temperature errors of 1D model and simplified model are both within 1.2 K in the first 18 s. The temperature rises more slowly in the experiment after 15 s. This may be influenced by temperature distribution inside a single cell, and heat dissipation to the ambient.

Comparison of one-dimensional model and simplified model.— Since internal states, such as membrane water distribution, ice fraction and reaction rate distribution, cannot be directly measured in the experiment, the simulation results of the 1D model are used as baseline to evaluate the accuracy of the simplified model.

The proposed simplified cold start model, Eqs. 41–65, is simulated on MATLAB, with a time step of 0.01 s. Operation conditions, geometry and material properties are the same as 1D model developed in this paper. Computation time is 20.88 s on the same platform, that is one order of magnitude faster. Simulation results are presented and compared with the 1D model in Fig. 12–Fig. 18.

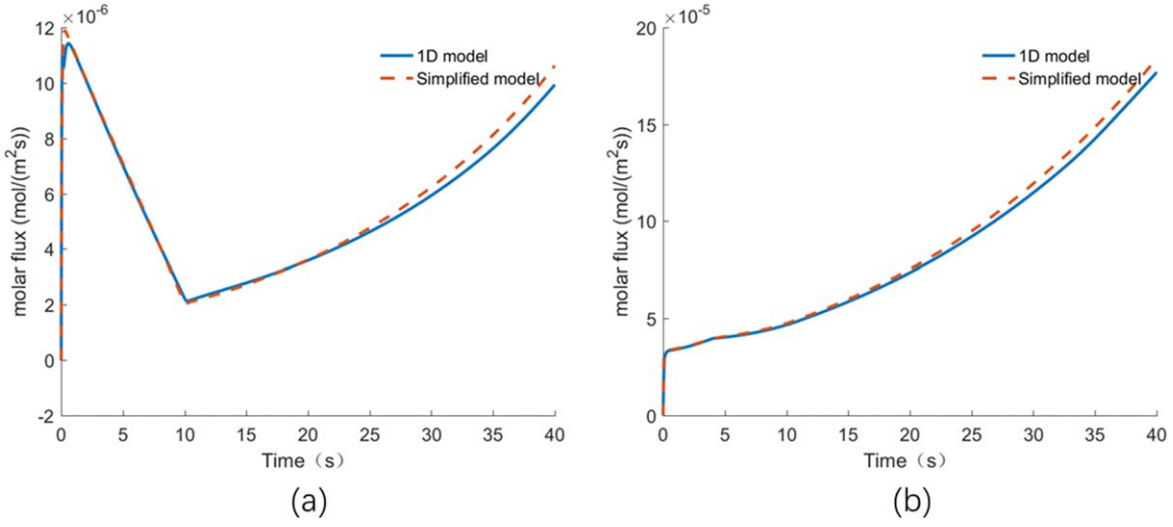

Figure 14. Comparison of water vapor flux in 1D model and simplified model: (a) from ACL to AGC, (b) from CCL to CGC.

Comparison of oxygen concentration is shown in Fig. 12, where average concentration is used in 1D model. Difference of oxygen concentration in CCL is within 3.87% during cold start, including the current ramping stage. Water vapor concentration inside fuel cell is quite low because of the low saturation pressure at low temperature. So water vapor flux is compared, as shown in Fig. 13. It is related to water removal from the cell, which is one of the key issues in fuel cell cold start. In 1D model, water flux at the GDL/GC interface is selected for comparison. Water vapor flux from ACL to AGC decreases in the beginning because water concentration in gas channel increases from zero, and membrane water content in ACL decreases at the beginning, the increase of water vapor flux in anode after 10 s and in cathode is caused by membrane water accumulation in MEA. The water flux differences of two models are within 8.02% and 6.26% (before 39 s) in anode and cathode respectively. Comparison of gas transport shows that the two models fit well, also verifying the static gas transport model assumption.

Membrane water distribution at different time is shown and compared in Fig. 14. The nonuniformity of membrane water distribution in MEA in the transient process is well described by the simplified model. Due to the strong electro osmotic drag, water content in ACL is much lower than in CCL. The five-region membrane water transport model is verified to be adequate to obtain the average water content in ACL, PEM and CCL, and also retains the nonuniformity of distribution at the same time.

Ice volume fraction evolution in CCL is presented and compared in Fig. 15. There are only two values of ice fraction in two regions of CCL in simplified model. The average values of ice fraction match well, while some of the detail of ice distribution in the part near membrane is lost.

Charge conservation in CCL is simplified into two reactions in two parts of CCL. The reaction percentage in the part near membrane is shown in Fig. 16. The maximum difference is 5.68%. The reaction rate distribution is influenced by total current density and ice fraction distribution. Influence of temperature is small because the temperature difference is very small inside the thin layer. Results show that reaction distribution in simplified model is close to 1D model, indicating that the simplification of electro chemical reaction in CCL is efficient.

Temperature distribution and average temperature in CCL are presented in Fig. 17 and Fig. 18. Temperature in simplified model fits well with the 1D model, with a difference within 0.25 °C. Average temperatures in CCL in the two models also match well as shown in Fig. 18.

Cell voltage is the result of many factors acting together. Comparison of cell voltage is shown in Fig. 20. Both models show the voltage reduction due to the current ramping and the voltage increase due to the temperature rise and membrane hydration. The maximum difference of cell voltage in two models is 0.0176 V (2.57%).

From the above comparisons of the two models, the simplified model shows a good match with 1D model, in gas transport, membrane water transport and phase change, electrochemical reaction and heat transfer. Static gas transport model is verified to be accurate enough to replace 1D transient gas transport model. Five-region model of membrane water in MEA can well describe the average water content and nonuniform distribution as well. Simplified model can describe ice formation in general but lose some of the detail in the part of CCL near membrane. Reaction simplification result also matches the baseline model result.

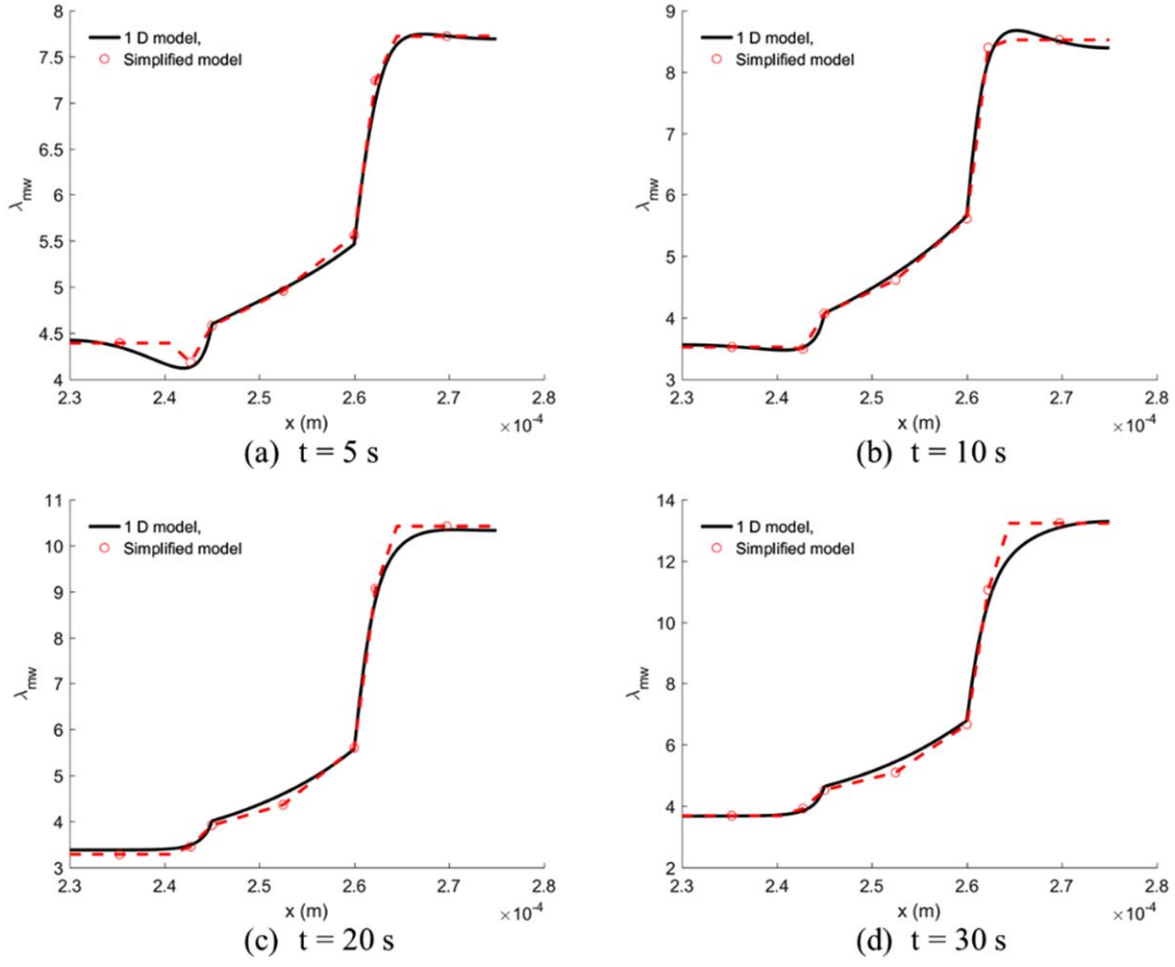

Figure 15. Comparison of membrane water distribution in 1D model and simplified model at different time.

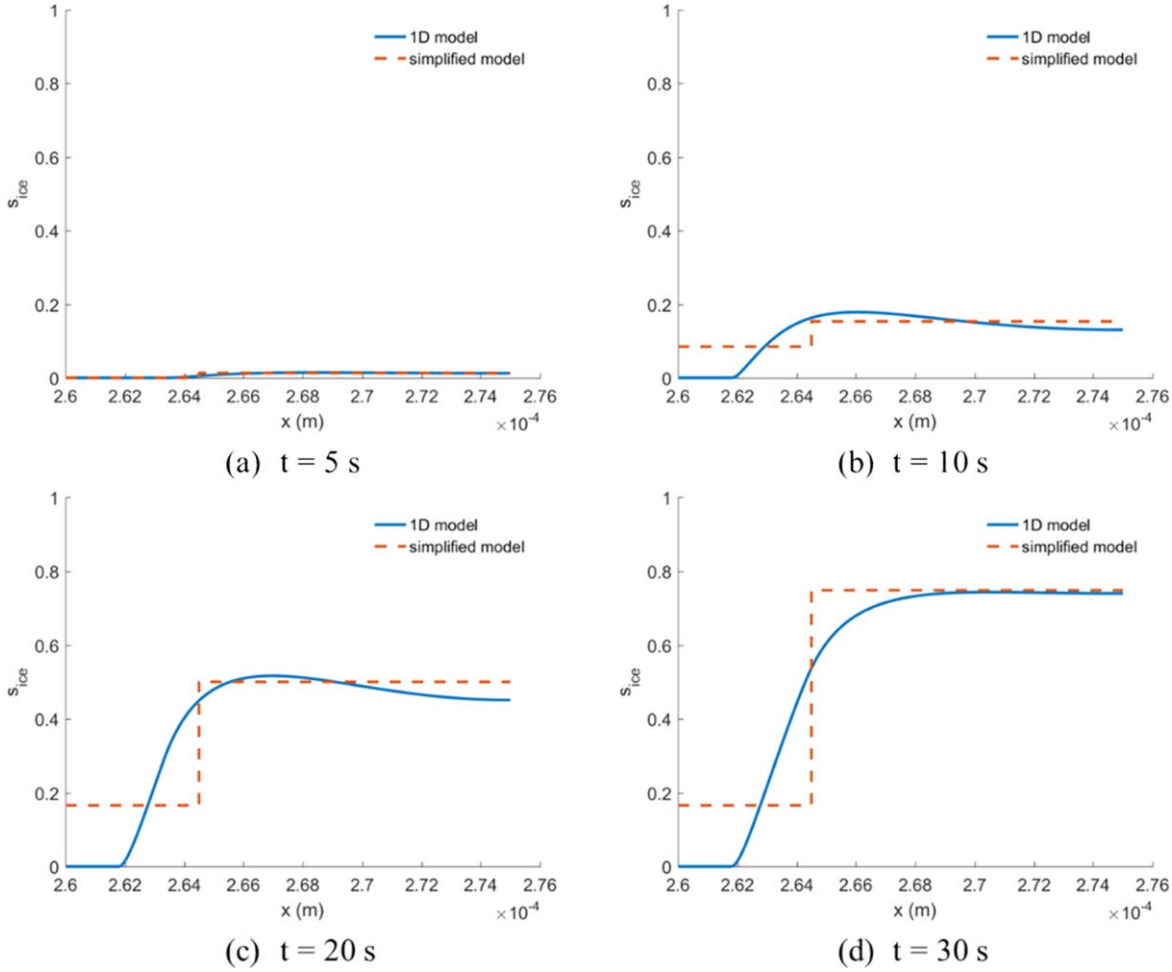

Figure 16. Comparison of ice volume fraction in 1D model and simplified model at different time.

According to the results, layer-lumped temperature model is adequate to simplify the 1D heat transfer model. As one of the most important output value and the results of all the multiphysics in fuel cell cold start, the cell voltage of the simplified model fits the voltage of the 1D model with an error within 0.0176 V. As for computational cost, the simplified model only takes about 1/10 of the time that 1D model needs, which is a significant improvement especially for larger scale modeling.

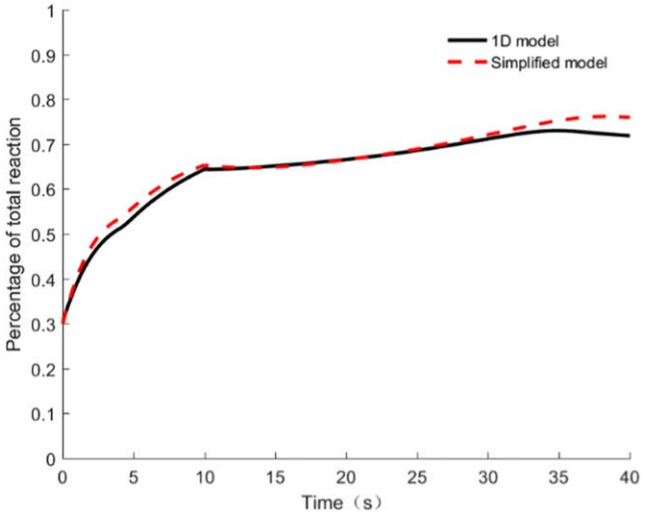

Figure 17. Comparison of reaction rate distribution in CCL in 1D model and simplified model.

Comparisons of simplified model and baseline 1D model are also conducted under different conditions (shown in Table V). Here, different initial temperatures, initial water contents, gas supply stoichiometric ratios are studied. Comparison results are listed in Table VI. Errors of gas transport results are less than 10% except for vapor flux in anode in case 2, in which initial water content $\lambda_0 = 3$ and water content in ACL is very low. For membrane water differences between simplified model and 1D model, errors of λ in region 7 (in CCL) are the largest of all regions, while errors in region 8 are the lowest. This results in low ice error in region 8, where most of the ice forms. Maximum temperature difference is 0.35 °C and maximum voltage difference is 0.026V. It can be concluded that the simplified model can be good approximate of 1D model under different operation conditions.

Conclusion

This paper has developed a 1D fuel cell cold start model and proposed a model dimension reduction simplification method. Both 1D model and simplified model were validated by cold start experiment data of a fuel cell stack, with cell voltage error within 15% and bipolar plate temperature error within 1.2 K. Comparing between 1D model and simplified model shows the accuracy of the simplified model, especially inhering the internal state distribution inside a single cell. Details of the conclusion are shown below.

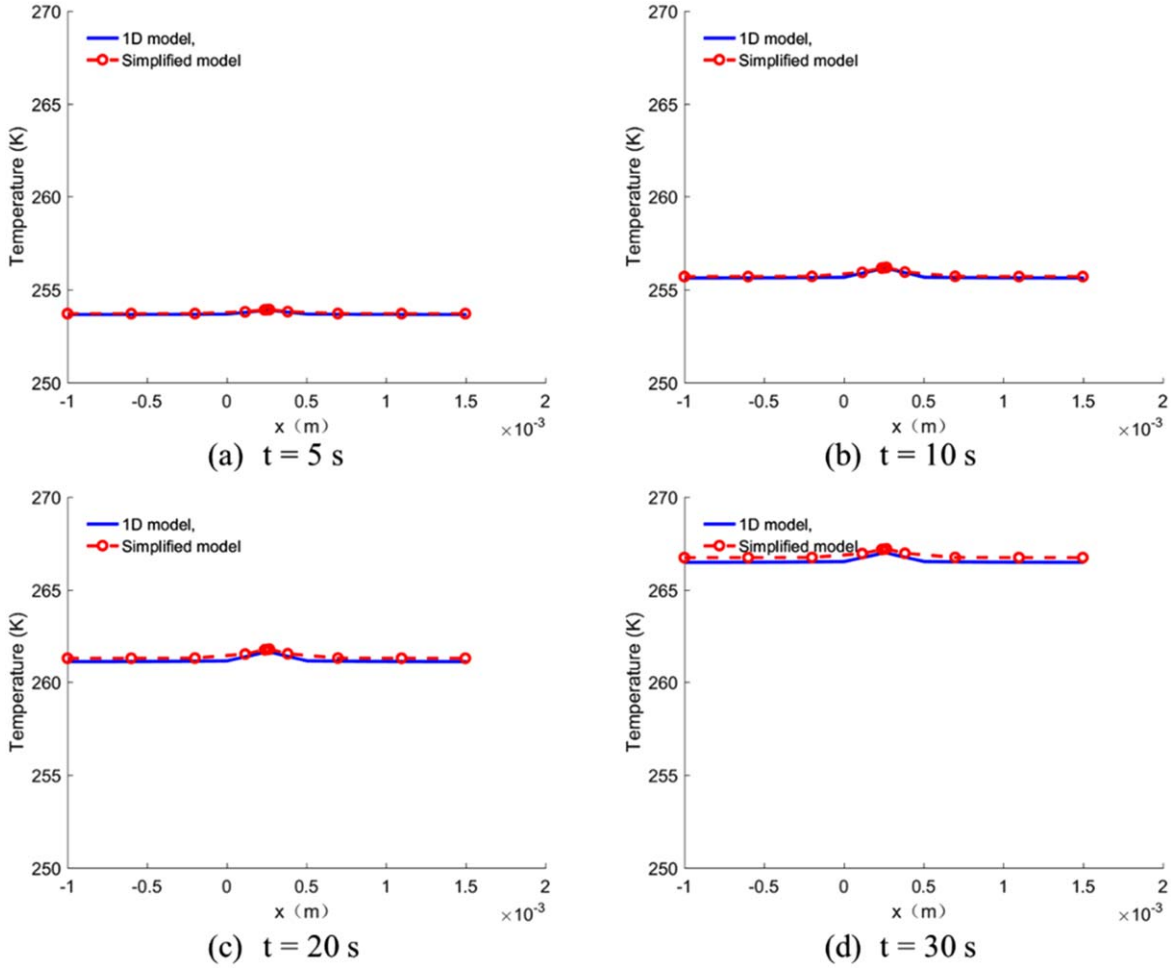

Figure 18. Comparison of temperature distribution in 1D model and simplified model at different time.

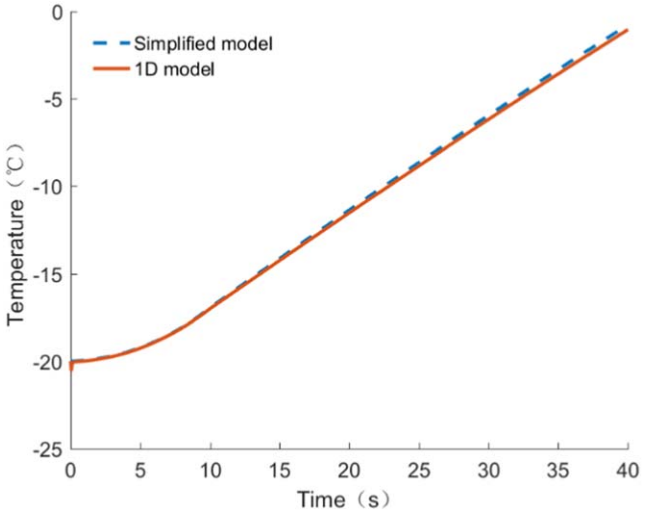

Figure 19. Comparison of average temperature in CCL in 1D model and simplified model.

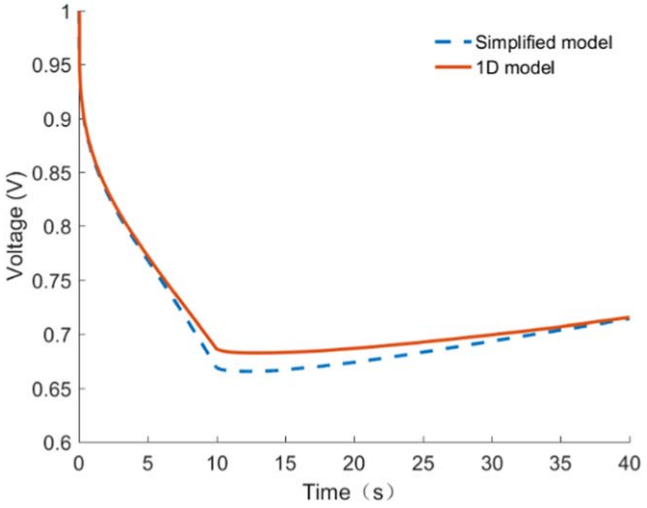

Figure 20. Comparison of cell voltage in 1D model and simplified model.

The 1D fuel cell cold start model describes the gas transport, water transport and phase change, electrochemical reaction, charge transport and heat transfer in through-plane direction. Simulation results show the main features of fuel cell cold start:

(1) Gas transport is mainly diffusion and much faster than membrane water transport.
(2) Distributions of reaction rate, membrane water and ice volume fraction are strongly nonuniform in CL.
(3) Ice mainly forms in CCL and from membrane water.
(4) The temperature distribution is basically linear inside each layer.

According to the results of the 1D model, dimension reduction simplification method was proposed to obtain a model with lower

Table V. Different conditions for model comparison.

Condition number	1	2	3	4
Initial temperature T_0(°C)	−20	−20	−15	−20
Initial water content in membrane λ_0	5	3	5	5
Anode stoichiometric ratio α_{H_2}	1.2	1.2	1.2	1.5
Cathode stoichiometric ratio α_{O_2}	1.5	1.5	1.5	2.0

Table VI. Maximum errors of simplified model under different conditions.

Condition number	1	2	3	4
Oxygen concentration in CCL	3.87%	3.9%	3.87%	4.97%
Vapor flux in anode	8.02%	12.8%	6.01%	6.81%
Vapor flux in cathode	6.26%	6.59%	2.54%	6.09%
Average water content in membrane	8.67%	8.54%	9.14%	8.60%
Average water content in region 4	5.49%	4.81%	4.71%	5.24%
Average water content in region 5	8.81%	7.87%	7.61%	8.57%
Average water content in region 7	9.57%	8.13%	11.53%	9.54%
Average water content in region 8	2.29%	9.25%	4.40%	2.25%
Ice saturation in region 7	0.0503	0.0062	0.0216	0.0504
Ice saturation in region 8	0.0584	0.0683	0.0797	0.0583
Reaction rate proportion in region 7	5.68%	6.16%	7.83%	5.67%
Temperature	0.25 °C	0.27 °C	0.35 °C	0.25 °C
Cell voltage	0.018 V	0.026 V	0.020 V	0.018 V
	2.57%	3.92%	2.87%	2.52%

computational cost. In this model, static gas transport model is used to replace the dynamic 1D gas transport model. ACL and CCL are both divided into two regions so a five region-model of membrane water in EMA is developed. Also ice fraction is simplified into two values in CCL. Reaction in CCL is divided into reactions in two regions to describe the reaction distribution. Lumped temperature values for all the layers in a single cell are used to approximate the 1D temperature distribution. Comparison between 1D model and simplified model results show that:

(1) Static gas transport model is verified to be accurate enough to replace 1D transient gas transport model, as the error of oxygen concentration in CCL and water vapor flux in anode and cathode are within 3.87%, 8.02% and 6.26% respectively.
(2) Five-region model of membrane water in MEA can well describe the average water content and nonuniform distribution as well. Simplified model can also describe ice formation in general but lose some of the detail in the part of CCL near membrane.
(3) Reaction simplification result also matches the baseline model result with a reaction percentage difference within 5.68%. Temperature difference is within 0.25 °C.And cell voltage of the simplified model fits the voltage of the 1D model with an error within 0.0176 V.
(4) Computation cost is significantly reduced through model simplification from 216 s to 20.88 s.
(5) Different conditions are used to study and compare the two models, and show the accuracy of the simplified model.

The proposed simplification method is verified to be valid and has good performance. The developed simplified model makes it possible to further integrate single cell model into large cell model and stack model. Some further researches are needed to improve the model, including optimization of parameters in different conditions, considering influence of Multi Porous Media (MPL), and liquid water modeling for flooding study after temperature rises above zero.

Acknowledgments

This work was supported by National Key R&D Program of China (No. 2018YFB0105600), National Natural Science Foundation of China (Nos. U1564209 and 51576113), Beijing Municipal Science & Technology Commission (No. Z181100004518004 and Z181100004518006). The support provided by China Scholarship Council (CSC) during a visit of Hongliang Jiang (CSC No. 201806210158) to University of Victoria is acknowledged.

References

1. L. Xu, U. Reimer, J. Li, H. Huang, Z. Hu, H. Jiang, H. Janßen, M. Ouyang, and W. Lehnert, *J. Power Sources*, **377**, 59 (2018).
2. J. Li, Z. Hu, L. Xu, M. Ouyang, C. Fang, J. Hu, S. Cheng, H. Po, W. Zhang, and H. Jiang, *Int. J. Hydrogen Energy*, **41**, 15295 (2016).
3. Y. Luo and K. Jiao, *Prog. Energy Combust. Sci.*, **64**, 29 (2017).
4. C. Wang, *Chem. Rev.*, **104**(10), 4727 (2004).
5. DOE, 2015, 1–58, https://energy.gov/sites/prod/files/2017/05/f34/fcto_myrdd_-fuel_cells.pdf (2016).
6. K. Kojima and K. Fukazawa, *ECS Trans.*, **69**, 213 (2015).
7. Y. Naganuma, K. Manabe, H. Imanishi, and Y. Nonobe, *SAE Int. J. Altern. Powertrains*, **1**, 2012-01–1230 (2012).
8. L. I. Jianqiu, F. Chuan, and X. U. Liangfei, *Automot. Saf. Energy*, **5**, 17 (2015).
9. Y. Hishinuma, T. Chikahisa, F. Kagami, and T. Ogawa, *Jsme Int. J. Ser. B-Fluids Therm. Eng.*, **47**, 235 (2004).
10. M. Oszcipok, D. Riemann, U. Kronenwett, M. Kreideweis, and M. Zedda, *J. Power Sources*, **145**, 407 (2005).
11. M. Oszcipok, M. Zedda, D. Riemann, and D. Geckeler, *J. Power Sources*, **154**, 404 (2006).
12. Q. Yan, H. Toghiani, Y. W. Lee, K. Liang, and H. Causey, *J. Power Sources*, **160**, 1242 (2006).
13. K. Tajiri, Y. Tabuchi, F. Kagami, S. Takahashi, K. Yoshizawa, and C. Y. Wang, *J. Power Sources*, **165**, 279 (2007).
14. K. Tajiri, Y. Tabuchi, and C.-Y. Wang, *J. Electrochem. Soc.*, **154**, B147 (2007).
15. S. Ge and C. Y. Wang, *Electrochim. Acta*, **52**, 4825 (2007).
16. S. Ge and C.-Y. Wang, *Electrochem. Solid-State Lett.*, **9**, A499 (2006).
17. Y. Tabe, K. Yamada, R. Ichikawa, Y. Aoyama, K. Suzuki, and T. Chikahisa, *J. Electrochem. Soc.*, **163**, F1139 (2016).
18. S. Ge and C.-Y. Wang, *J. Electrochem. Soc.*, **154**, B1399 (2007).
19. Y. Wang, P. P. Mukherjee, J. Mishler, R. Mukundan, and R. L. Borup, *Electrochim. Acta*, **55**, 2636 (2010).
20. Y. Ishikawa, H. Hamada, M. Uehara, and M. Shiozawa, *J. Power Sources*, **179**, 547 (2008).
21. N. Wakatake, Y. Tabe, and T. Chikahisa, *in ECS Transactions*, **75**, 623 (2016).

22. I. Mayrhuber, F. Marone, M. Stampanoni, T. J. Schmidt, and F. N. Büchi, *ChemElectroChem*, **2**, 1551 (2015).
23. L. Mao and C.-Y. Wang, *J. Electrochem. Soc.*, **154**, B139 (2007).
24. Y. Wang, *J. Electrochem. Soc.*, **154**, B1041 (2007).
25. F. Huang, *Thesis*, Tsinghua University (2018).
26. T. J. Dursch, M. A. Ciontea, C. J. Radke, and A. Z. Weber, *Langmuir*, **28**, 1222 (2012).
27. T. J. Dursch, M. A. Ciontea, G. J. Trigub, C. J. Radke, and A. Z. Weber, *Int. J. Heat Mass Transf.*, **60**, 450 (2013).
28. T. J. Dursch, G. J. Trigub, J. F. Liu, C. J. Radke, and A. Z. Weber, *Int. J. Heat Mass Transf.*, **67**, 896 (2013).
29. Y. Ishikawa, M. Shiozawa, M. Kondo, and K. Ito, *Int. J. Heat Mass Transf.*, **74**, 215 (2014).
30. F. Jiang, W. Fang, and C.-Y. Wang, *Electrochim. Acta*, **53**, 610 (2007).
31. L. Mao, C.-Y. Wang, and Y. Tabuchi, *J. Electrochem. Soc.*, **154**, B341 (2007).
32. K. Jiao and X. Li, *Electrochim. Acta*, **54**, 6876 (2009).
33. J. Macedo-Valencia, J. M. Sierra, S. J. Figueroa-Ramirez, S. E. Diaz, and M. Meza, *Int. J. Hydrogen Energy*, **41**, 23425 (2016).
34. R. K. Ahluwalia and X. Wang, *J. Power Sources*, **162**, 502 (2006).
35. R. J. Balliet and J. Newman, *J. Electrochem. Soc.*, **158**, B927 (2011).
36. R. J. Balliet and J. Newman, *J. Electrochem. Soc.*, **158**, B1142 (2011).
37. R. Balliet and J. Newman, *ECS Trans.*, **33**, 1545 (2010).
38. A. Nandy, F. Jiang, S. Ge, C.-Y. Wang, and K. S. Chen, *J. Electrochem. Soc.*, **157**, B726 (2010).
39. S. He, S. H. Kim, and M. M. Mench, *J. Electrochem. Soc.*, **154**, B1024 (2007).
40. M. Sundaresan and R. M. Moore, *J. Power Sources*, **145**, 534 (2005).
41. M. Sundaresan, *Thesis*, University of California, Davis (2004).
42. M. Khandelwal, S. Lee, and M. M. Mench, *J. Power Sources*, **172**, 816 (2007).
43. Y. Zhou, Y. Luo, S. Yu, and K. Jiao, *J. Power Sources*, **247**, 738 (2014).
44. L. Xu, C. Fang, J. Li, M. Ouyang, and W. Lehnert, *Appl. Energy*, **230**, 106 (2018).
45. Y. Qi, M. Espinoza-Andaluz, M. Thern, and M. Andersson, *eTransportation*, **2**, 100030 (2019).
46. K. H. M. Al-Hamed and I. Dincer, *eTransportation*, **2**, 100027 (2019).
47. C. Fang, *Thesis*, Tsinghua University (2017).
48. J. Hu, J. Li, L. Xu, F. Huang, and M. Ouyang, *Energy*, **111**, 869 (2016).
49. T. Tang, S. Heinke, A. Thüring, W. Tegethoff, and J. Köhler, *Int. J. Hydrogen Energy*, **42**, 15328 (2017).
50. F. Jiang, W. Fang, C.-Y. Wang, L. Mao, C.-Y. Wang, Y. Tabuchi, K. Tajiri, Y. Tabuchi, and C.-Y. Wang, *J. Electrochem. Soc.*, **154**, B341 (2007).
51. K. Jiao and X. Li, *Prog. Energy Combust. Sci.*, **37**, 221 (2011).
52. S. Motupally, A. J. Becker, and J. W. Weidner, *J. Electrochem. Soc.*, **147**, 3171 (2002).
53. T. A. Zawodzinski, *J. Electrochem. Soc.*, **140**, 1041 (1993).
54. T. A. Z. T. E. Springer and S. Gottesfeld, *J. Electrochem. Soc.*, **138**, 2334 (1991).
55. J. T. Hinatsu, *J. Electrochem. Soc.*, **141**, 1493 (2006).
56. C. Bao and W. G. Bessler, *J. Power Sources*, **275**, 922 (2015).
57. E. L. Thompson, T. W. Capehart, T. J. Fuller, and J. Jorne, *J. Electrochem. Soc.*, **153**, A2351 (2006).
58. A. Kulikovsky, *eTransportation*, **2**, 100026 (2019).
59. J. Huang and J. Zhang, *J. Electrochem. Soc.*, **163**, A1983 (2016).